Acta Materialia 257 (2023) 119147

Contents lists available at ScienceDirect

Acta Materialia

journal homepage: www.elsevier.com/locate/actamat

Full length article

Segregation of Yttrium at the Mg/MgO interface in an Mg-0.5Y Alloy

Shihao Wang [a,*], Yun Wang [a], Quentin M. Ramasse [b,c], Rainer Schmid-Fetzer [d], Zhongyun Fan [a]

[a] BCAST, Brunel University London, Uxbridge, Middlesex UB8 3PH, UK
[b] SuperSTEM Laboratory, SciTech Daresbury Campus, Daresbury WA4 4AD, UK
[c] School of Chemical and Process Engineering and School of Physics, University of Leeds, Leeds LS2 9JT, UK
[d] Institute of Metallurgy, Clausthal University of Technology, Robert-Koch-Str. 42, D-38678, Clausthal-Zellerfeld, Germany

ARTICLE INFO

Keywords:
Metal/Oxide Interface
Interfacial Segregation
Heterogeneous Nucleation
Aberration-corrected Scanning Transmission Electron Microscopy
Magnesium alloys

ABSTRACT

Interfacial segregation of selected elements can be exploited to manipulate the potency of solid substrates for heterogeneous nucleation, thus controlling the solidification process. As the native inclusions in Mg alloys, MgO acts as the nucleating substrate, but it has rarely been studied in terms of its interactions with alloying elements. In this work, investigations of yttrium (Y) segregation at interfaces between native MgO particles and Mg in an Mg-0.5Y alloy were carried out by state-of-the-art aberration-corrected scanning transmission electron microscopy (STEM) and associated spectroscopy. Experimental results show that native MgO particles in Mg-0.5Y possess two typical morphologies: truncated octahedron primarily faceted by $\{111\}_{MgO}$ and minorly by $\{100\}_{MgO}$, and cubic shape with unique $\{100\}_{MgO}$ facets. Y atoms are found to segregate at both Mg/$\{111\}_{MgO}$ and Mg/$\{100\}_{MgO}$ interfaces, leading to the formation of two different 2-dimensional compounds (2DCs). The 2DC at the Mg/$\{111\}_{MgO}$ interface is identified as two atomic layers of a face-centered cubic Y_2O_3 phase in terms of crystal structure and chemistry, whilst it is an Mg(Y)-O monolayer at the Mg/$\{100\}_{MgO}$ interface, coherently matching with the terminating $\{100\}_{MgO}$ plane. Discussion is focused on the mechanisms underlying the formation of the 2DCs, their effects on the nucleation potency of MgO particles, and grain refinement. This work sheds light on how heterogeneous nucleation can be manipulated by altering the nucleation potency of a substrate through deliberately promoting elemental segregation of carefully chosen element(s).

1. Introduction

Heterogeneous nucleation during the solidification of metallic materials is essential for engineering the solidification structure and hence the properties of the final casting [1]. As a common industrial practice, chemical inoculation of potent particles is applied to achieve a fine and uniform grain structure by promoting heterogeneous nucleation [1,2]. Based on the spherical cap model, heterogeneous nucleation is described as a thermally activated stochastic process by the classical nucleation theory (CNT) [3]. However, CNT is not valid when nucleation occurs on a potent substrate with a small contacting angle (*e.g.*, smaller than 20 degrees) [4]. Previous studies have shown that it is more reasonable to treat heterogeneous nucleation as the dynamic adsorption of liquid atoms [4], which is a deterministic and athermal process [5–7]. Recent studies on the atomistic mechanism of nucleation realize that the potency of a substrate for heterogeneous nucleation is closely related to the lattice misfit at the solid/substrate interface [2,7-9], the chemical interaction between the substrate and the liquid atoms [10–16] and the substrate's atomic-level surface roughness [13,17]. Therefore, the atomic configuration and chemical composition at the substrate surface play a major role in determining nucleation behaviour and thus, the solidification structure.

Segregation of element(s) at generic interfaces is a widespread phenomenon, which is driven by the decrease in interfacial energy, as described by the Gibbs adsorption isotherm [18–20]. Generally, the physical and chemical conditions on a substrate surface can be altered by the interfacial segregation of various alloying elements or impurities present in the alloy melt. One of the consequences is the formation of interfacial layers which are different from the substrate in terms of structure and/or chemistry, leading to the modification of the substrate surface and thus to the variation of nucleation potency. It is therefore feasible to manipulate the potency of a substrate through interfacial segregation of selected elements. This acts as a mechanism for the grain refining behaviour, as elucidated by experimental observations and by theoretical models and simulations [9,10,13,14,21-27]. The potency variations of TiB_2 serve as excellent examples to demonstrate how a

* Corresponding author.
E-mail address: swang@superstem.org (S. Wang).

https://doi.org/10.1016/j.actamat.2023.119147
Received 2 April 2023; Received in revised form 3 July 2023; Accepted 8 July 2023
Available online 11 July 2023

substrate's potency is manipulated by interfacial segregation. The $\{0001\}_{TiB2}$ surface has a misfit of -4.2 % with the $\{111\}_{Al}$ plane at 660ºC along the close-packed directions [25], suggesting that TiB_2 is not highly potent for nucleating αAl. Segregation of Ti solute atoms at the liquid-Al/TiB_2 interface leads to the formation of an Al_3Ti two-dimensional compound (2DC) monolayer, which reduces the absolute lattice misfit to 0.09 % and hence increases the nucleation potency [25]. By contrast, the addition of 580 ppm Zr destabilizes the Al_3Ti 2DC, which disappears and a Ti_2Zr 2DC monolayer forms instead on the $\{0001\}_{TiB2}$ surface [13]. The Ti_2Zr 2DC has not only a large misfit with Al but also an atomically rough surface, making such TiB_2 particles impotent for αAl nucleation.

As the predominant inclusions in magnesium (Mg) and Mg alloys, native magnesia (MgO) nanoparticles have been successfully applied for grain refinement, despite the relatively low potency due to a 7.9 % lattice misfit with Mg and the atomically rough surface [12,28-35]. Native MgO has a mean size below 100 nm, a narrow lognormal size distribution, and a number density level of $10^{17}/m^3$ after dispersion by high shear melt conditioning (HSMC) [30,35]. According to the grain initiation map [34], the impotent MgO particles nucleate and initiate Mg grains majorly in an explosive grain initiation manner, being able to achieve better grain refinement than the more potent nucleant particles do. Unlike the Zr-containing grain refiner with applications limited to Al-free Mg alloys, native MgO particles have shown their refining capabilities in various Mg alloys [27,28,33,36]. Making use of native oxide particles is an attractive and efficient way to promote the integrity of castings.

Interactions between the segregated solutes and the native MgO particles are expected in an Mg alloy melt at the processing temperature. For instance, minor addition of Sr [37], Zr [21] and Ca [27,36] to Mg melts was shown to interact with native MgO particles and thus alter their nucleation potency, resulting in varying levels of grain refinement of Mg alloys. Unfortunately, we still know little about how different alloying elements interact with MgO particles and how the substrate's potency is altered accordingly. It becomes crucial to understand the elemental segregation behaviour at the Mg/MgO interfaces, and thus to make full use of the native MgO as a universal grain refiner for Mg alloys.

Yttrium (Y) is an important alloying element for advanced Mg alloys, whose addition has been shown to lead to multiple improvements, such as strength [38], ductility [39], creep resistance [40] and oxidation resistance [41]. Although the Mg-Y binary system has been often used as a model system for the Mg-rare earth (RE) alloys, little work has been carried out on investigating the effect of Y addition on the grain size of Mg alloys. A previous study showed that the addition of low-grow-restriction Y appears to have a marginal effect on grain refinement of Mg alloys [42], and other investigations were focused on grain refinement of the WE series alloys (based on Mg-Y) using Mg-Zr master alloys [43].

The objective of this work is to reveal the segregation behaviour of Y at the Mg/MgO interfaces and the consequent effects on the nucleation potency of MgO. With dedicated aberration-corrected scanning transmission electron microscopy (STEM) and associated spectroscopy, the investigation focuses on the characterisation of Mg/MgO interfaces with and without the segregation of Y down to atomic precision, elucidating the structure and chemistry of interfacial segregation layers. The discussion is concentrated on the segregation behaviour of Y and the mechanisms for the formation of 2DCs at the interfaces. The effects of Y-segregation-induced 2DCs on the nucleation potency of MgO particles and the grain refinement behaviour will be analysed as well. This work sheds light on manipulating nucleation potency through elemental segregation at the liquid/substrate interface.

2. Experimental

2.1. Materials

Commercial purity magnesium (CP Mg) and pure yttrium (Y) were used as the raw materials in this work. Table 1 gives the compositions (all compositions are in wt.% unless otherwise specified) and the impurity levels.

2.2. Grain size assessment

Under the protective atmosphere of N_2 containing 0.4 vol% SF_6, about 1 kg of CP Mg was melted at 700 °C in a steel crucible using an electric resistance furnace. An Mg-0.5Y alloy melt was made by adding pure Y into the CP Mg melt, with manual stirring and isothermal holding for at least an hour to ensure the dissolution of Y. We used the standard TP-1 test [44] to assess the grain refining performance, where the test provided consistent solidification conditions, ensuring a cooling rate of 3.5 K/s at the central region of a cross-section 38 mm from the bottom of the TP-1 sample. The CP-Mg and Mg-0.5Y alloy melts were then cooled down to 680 °C. One set was directly cast into a TP-1 mould pre-heated at 350 °C, which was transferred to a cooling unit with water spray flowing at the rate of 3.8 L/min. The solidified samples were denoted as CPMg-TP1, and Mg-0.5Y-TP1, respectively. While the other set was treated by high shear melt conditioning (HSMC) for 5mins at 4000 rpm prior to the TP-1 casting, by which the obtained samples were denoted as CPMg-HSMC-TP-1 and Mg-0.5Y-HSMC-TP-1, respectively.

Examination of grain structure and quantitative measurement of the grain size were carried out on both the cross section 38 mm from the base and the longitudinal section of the solidified TP-1 ingots. Specimens were prepared following standard metallographic procedures. Chemical etching was performed with an acetic-picral solution consisting of 10 ml acetic acid, 4.2 g picric acid, 10 ml H_2O and 140 ml ethanol. Optical macrography and micrography were carried out using an Epson image scanner and a Zeiss optical microscope (OM), respectively. The quantification of the columnar grain width and equiaxed grain size of the samples was conducted according to the mean linear intercept method (ASTM E112-10).

2.3. Characterization of MgO and Mg/MgO interfaces

A pressurized melt filtration technique was used to concentrate oxide particles from the melts to facilitate microstructural examination. During the filtration process, 1 kg of CP-Mg or Mg-0.5Y alloy melt was transferred to the pre-heated filtration unit (the Footprinter, ABB Inc.) isolated from the air. Argon was introduced with a sufficiently high pressure to force the melt to flow through the porous ceramic filter located at the bottom of the crucible. This allows the oxide particles to be accumulated above the ceramic filter. The residual melt (about 150 g) containing concentrated oxides then solidified in the crucible. The details of the filtration technique were presented elsewhere [28]. This technique was successfully used to study nucleant particles in various Al- and Mg- alloys [13,25,27,28].

Samples for scanning electron microscopy (SEM) were made from the remnant materials above the filter where the oxide particles were concentrated. The morphology and chemistry of collected oxide particles in the samples were examined by SEM using a Carl Zeiss Crossbeam 340 microscope equipped with the detector for energy-dispersive X-ray spectroscopy (EDS).

Samples for scanning transmission electron microscopy (STEM) and electron energy-loss spectroscopy (EELS) were made from slices cut from the residual materials above the filter. The slices were mechanically ground to 60 μm in thickness and then punched into ϕ3 mm discs, which were finally thinned by Ar ion beam in a Gatan Precise Ion Polishing System. Applied beam voltages ranged from 1 to 5 kV and the beam angles from 3 to 5 degrees. Preliminary sample screening was

Table 1
Compositions (wt.%) of the materials used in this work.

Alloy	Al	Zn	Mn	Si	Fe	Cu	Ni	Be	Mg	Supplier
CP Mg	0.019	0.002	0.032	0.013	0.002	<0.001	<0.001	<0.0001	Balance (>99.9)	Magontec Ltd
Pure Y	Y>99.9									Fisher Scientific UK Ltd

done on a JEM 2100F microscope operated at 200 kV. Dedicated characterisation with STEM/EELS was carried out using a Nion UltraSTEM100 instrument at the EPSRC-UK SuperSTEM laboratory. The microscope was operated at an accelerating voltage of 100 kV, with the probe forming optics configured for a 31 mrad convergence semi-angle and a probe size of 1 Å. The collection semi-angle ranges for all high-angle annular dark-field (HAADF) and medium-angle annular dark-field (MAADF) STEM mages were 89-195 mrad and 52-89 mrad, respectively. The microscope is equipped with a Gatan Enfina spectrometer for chemical analysis by EELS, with a collection semi-angle of 36 mrad. EELS spectrum images (EELS SI) were acquired by recording EELS spectra at each pixel across a defined area of the specimen. Noise reduction of EELS SI data was conducted by application of principal component analysis (PCA), as implemented in the HREM Research MSA plugin for Digital Micrograph [45].

Additional atomic-resolution STEM/EDS mapping was carried out on a JEM-ARM300F2 GRAND ARM™2 equipped with large-size EDS dual detectors. A Thermo Fisher Spectra300 was used for the acquisitions of simultaneous HAADF and integrated differential phase contrast (iDPC) STEM images. Both microscopes were operated at 300 kV.

Simulation of HAADF STEM images was conducted using the QSTEM software package developed by Koch [46] according to the atomic structure models of the interfacial segregation layers derived from experimental STEM and EELS results. The experimental parameters including beam convergence, detector inner and outer radii were used as input for the simulations. A total of 15 frozen phonons were considered, and probe size effects were included by convoluting the images with a 1 Å (full width at half-maximum) Gaussian distribution. The simulated HAADF images were compared with experimental data to validate the derived atomic structure and chemistry of the segregation layers.

3. Results

3.1. Morphology and size of native MgO particles

Native MgO particles are the predominant inclusions in CP Mg and Mg-Al alloys [30], which is the same case in the Mg-0.5Y alloy. Bulk Y_2O_3 phases were rarely observed, while the $Mg_{24}Y_5$ intermetallic

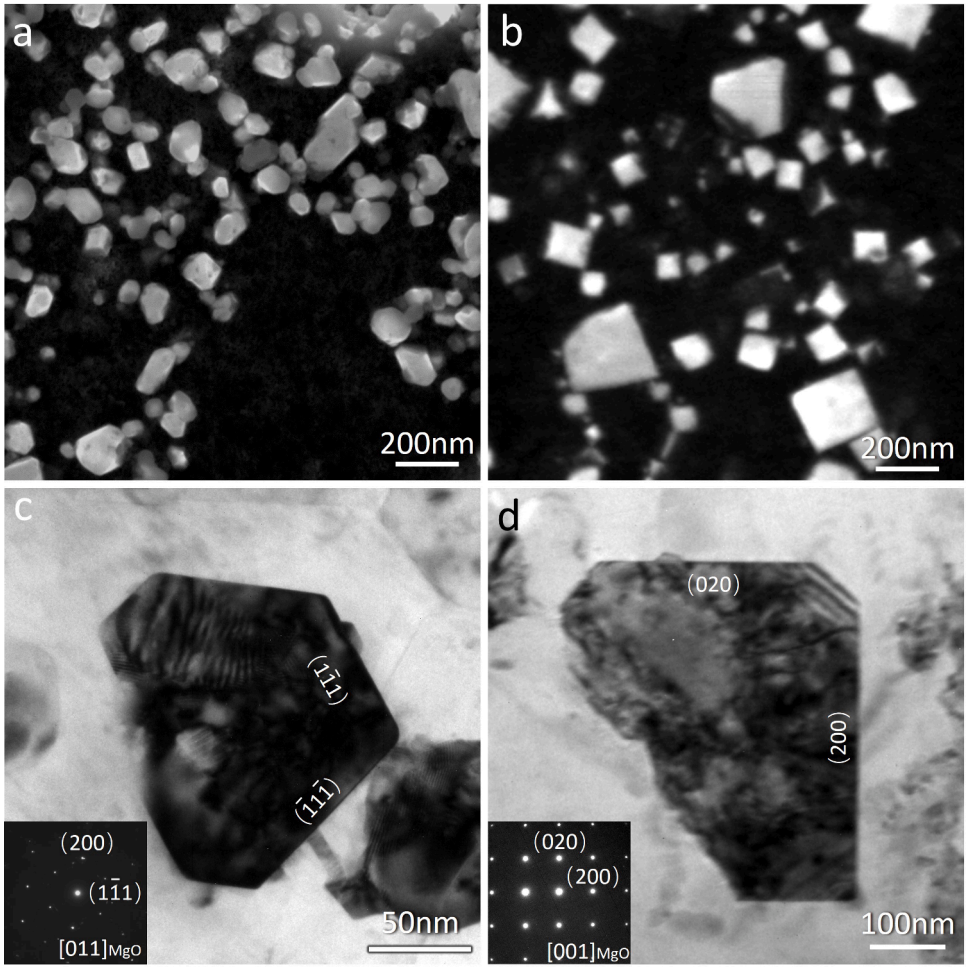

Fig. 1. Native MgO particles collected from the Mg-0.5Y melt. (a-b) SEM micrographs showing the (a) (truncated) octahedral and (b) cubic morphologies of MgO particles; and (c-d) TEM bright field images and corresponding electron diffraction patterns (inserts) showing their crystallographic features. (c) truncated octahedral MgO is faceted primarily by {111}, while (d) cubic MgO is faceted by {100} only.

phase, which has been considered a potent substrate for nucleating αMg [47], was not detected in Mg-0.5Y in this work. Comparing the MgO particles in CP Mg and Mg-0.5Y (Fig. 1 and Fig. S1), we notice that the addition of 0.5Y into the CP Mg melt shows little impact on the native MgO particles in terms of phase stability, crystal morphology and size. As shown in Fig. 1, nano-sized MgO particles are the only components for the young oxide films collected from the melt of Mg-0.5Y. They appear as two typical morphologies: truncated octahedral (or octahedral, in Fig. 1(a) and (c)) and cubic shapes (Fig. 1(b) and (d)). The polyhedral appearance of the particles in Fig. 1(a) can be understood as the random projections in two dimensions of the truncated octahedral particles [30]. The extensive SEM characterisation suggests that the octahedral and truncated octahedral MgO particles are predominant in terms of number density. The crystallographic features are well interpreted by the bright-field (BF) TEM images and the corresponding selected area electron diffraction (SAED) patterns (Fig. 1(c) and (d)). The truncated octahedral MgO, viewed along $[011]_{MgO}$, is faceted primarily by {111} and to a lesser extent by {100} planes (as the result of incomplete growth), which can be, hereafter, denoted as {111} MgO. With the viewing direction parallel with $[100]_{MgO}$, the cubic MgO exhibits a unique crystallographic termination of {100} planes, which is denoted as {100} MgO. Therefore, we conclude that the primary inclusions in Mg-0.5Y are native MgO nanoparticles of two morphologies: {111} MgO and {100} MgO, as the same conclusions hold in CP Mg [30].

3.2. Confirmation of the segregation of Y at the Mg/MgO interfaces

Differences between the native MgO particles in CP Mg and Mg-0.5Y are noticed at the Mg/MgO interfaces revealed by advanced electron microscopy. Fig. 2 characterises the Mg/$\{111\}_{MgO}$ interface for a {111} MgO particle and the Mg/$\{100\}_{MgO}$ interface for a {100} MgO particle in Mg-0.5Y by HAADF and MAADF STEM imaging. Owing to the differences in atomic number for elements (Z_Y=39, Z_{Mg}=12, Z_O=8) in the studied system, the Z-sensitive HAADF STEM imaging is an effective technique to study the potential chemical segregation at the Mg/MgO interfaces after Y addition. In addition, MAADF STEM imaging provides additional strain contrast by collecting electrons scattered to lower angles and thus containing a higher fraction of elastic scattering. In direct comparisons to the featureless Mg/MgO interfaces in CP Mg (Fig. S1(c) and (f)), brighter layers are observed at both the Mg/$\{111\}_{MgO}$ and Mg/$\{100\}_{MgO}$ interfaces in Mg-0.5Y (Fig. 2 (a) and (d)). The Z-contrast interpretation suggests that the interfacial layers contain Y atoms, as Y is the species with the highest atomic number present in the system. The invariance in the morphologies of MgO particles/films suggests that the native MgO films/particles in CP Mg experience a fine-scale interaction with Y solutes at the Mg/MgO interfaces after the addition of 0.5Y. The presence of 0.5Y in the Mg melt is thus thought to have led to the formation of Y-rich segregation layers at the Mg/MgO interfaces. The composition will be further confirmed by EELS analysis. In addition, the lattice periodicity of MgO disrupts locally at the Y-rich interfacial layers, giving rise to a static displacement contribution to the electron

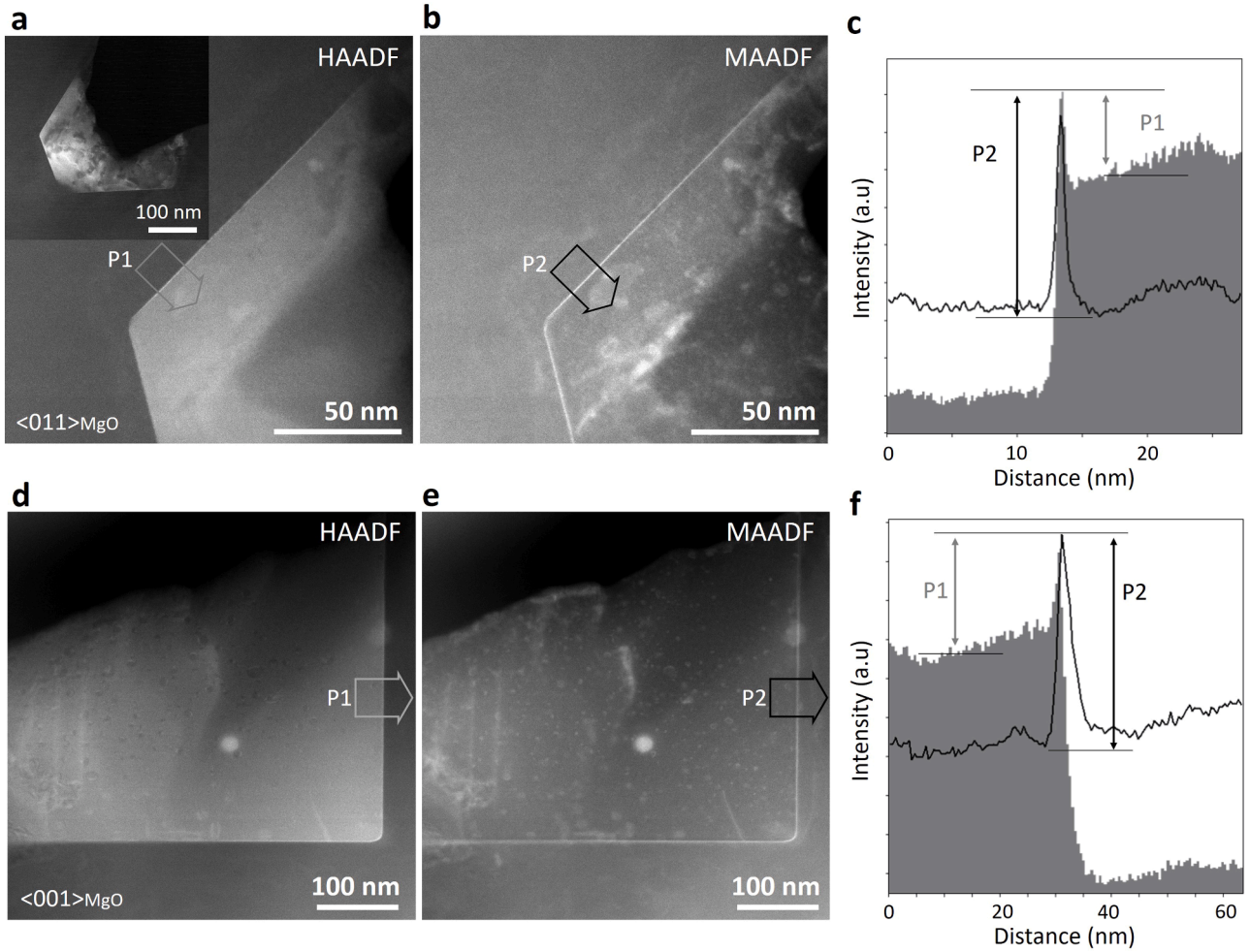

Fig. 2. HAADF/MAADF STEM images and the corresponding contrast profiles showing the segregation of Y at the Mg/MgO interfaces. (a-c) Mg/$\{111\}_{MgO}$ interface; and (d-f) Mg/$\{100\}_{MgO}$ interface. (c) and (f) are the contrast profiles along the marks 'P1'/'P2' across the interfaces.

scattering, which corresponds to extra contrast in the MAADF STEM images (Fig. 2(c) and (f)). Besides, the segregation of Y at the Mg/MgO interfaces is general in Mg-0.5Y, as Y was readily detected in association with most MgO particles by SEM/EDS (Fig. S2).

3.3. Segregation of Y at the Mg/{111}$_{MgO}$ interface

Segregation of Y at the Mg/{111}$_{MgO}$ interface is further verified by EELS analysis. Fig. 3(a) compares the EELS spectra acquired from Mg ('1'), interface ('2'), and MgO ('3'), among which the Y $L_{2,3}$ core loss edges are only detectable at the interface. The spatial distribution of Y is revealed by comparing EELS elemental maps and the simultaneously acquired atomic-resolution HAADF STEM contrast in Fig. 3(b). The presence of Y coincides with the two brighter interfacial layers, at which Mg is seen to be depleted. Structurally, the disruption in lattice periodicity is seen at the interface: a quasi-square pattern is recognised for the Y-rich segregation layers, which is different from the structure of MgO. Other trace elements are less likely to segregate as no impurity elements of significance can be detected at the Mg/MgO interface in CP Mg (Fig. S3). It is now verified that Y segregates at the Mg/{111}$_{MgO}$ interface, forming two Y-rich atomic layers.

Figure 4 reveals in more detail the atomic structure of the Y-rich segregation layers at the Mg/{111}$_{MgO}$ interface by atomic-resolution HAADF and BF STEM images acquired along the $[2\bar{1}1]_{MgO}$ zone axis. Clearly, the Y-rich segregation layers have a different structure from the MgO matrix. In both Fig. 4(a) and (b) a near-square periodicity (black square annotation) is observed for the Y-rich atomic columns over a wide range of the interfacial layers, whilst MgO has a rectangle structure unit (white rectangle annotation). Domain matching epitaxy [48] is seen at the interface: 11 $(011)_{MgO}$ atomic planes match 12 atomic planes of the Y-rich layers. With the MgO matrix as the internal reference for the measurement [49], the average size of the quasi-square pattern of the Y-rich columns is 2.73±0.1 Å in width (along the interface) and 2.63 ±0.1 Å in height (perpendicular to the interface). It is noted that the value 2.63 Å is almost identical to the {200} interplanar spacing for an FCC Y_2O_3 crystal (nominally 2.632 Å,) [50]. An additional epitaxial layer rich in Mg (as deduced from the EELS analysis in Fig. 3(b)) can be distinguished right above the Y-rich layers, having the same arrangement as Y-rich columns whilst similar contrast as the Mg columns inside the MgO (Fig. 3(b) and Fig. 4). It is suggested that this could be the fingerprint inherited from the prenucleation process of αMg, which shall warrant further dedicated work. Due to oxygen's low Z number, O columns are often invisible by HAADF imaging. However, some dark-contrast columns are visible in the corresponding BF STEM images (Fig. 4(b) and (d)), whose equivalent positions on Fig. 4(c) are the centres of the quasi squares. This suggests that O is present in the Y-rich segregation layers, which will be confirmed later by EELS examinations (Fig. 5). The STEM/EDS maps across the Mg/{111}$_{MgO}$ interface (Fig. S4) show that O signal is detected at the location of Y-rich layers, where the O intensity is visibly stronger than that in the Mg matrix. Besides, the original Mg-terminating {111} atomic layer is replaced by the Y-rich atomic layers, leaving an oxygen atomic layer between the Y-rich segregation layers and MgO matrix (Fig. 4(b) and (d)).

Given such a thin Y-rich segregation layer, the possible contributions to the recorded Mg and O intensity of delocalized inelastic scattering from the adjacent Mg and MgO phases during EELS acquisitions make it difficult to quantify the chemical composition merely based on peak intensities. Nevertheless, the electron energy-loss near-edge structure (ELNES) of the corresponding core-loss edges provides indications about the bonding information of the atoms within the segregation layer and across the Mg/MgO interface. Fig. 5 compares the EELS spectra acquired from the five locations (marked by lines '1' to '5' with different colours) across the interface, verifying the involvement of O in the Y-rich interfacial layers. The intensity of the O K edge in spectrum '4' (interfacial layers) is lower than that in spectra '1' to '3' (MgO) but much stronger than that in spectrum '5' (corresponding to the Mg matrix: here, any non-zero O K intensity is attributed to the oxidation on the specimen surface). Furthermore, the ELNES of O K edges gradually evolves into two peaks upon approaching the interface (as indicated by dashed lines) until the position where the ELNES closely resembles the O K fine structure of a standard Y_2O_3 EELS spectrum [51]. This strongly suggests that O atoms exist between the two Y atomic layers and that the bonding environment of the Y atoms in the segregation layer is similar to that of Y atoms in a bulk Y_2O_3 crystal, *i.e.*, Y-O bond.

The ELNES of the Mg K edge was also examined to verify if Mg is involved in the Y-rich segregation layers. Fig. 6 shows the EELS spectra from three locations across the interface (marked by regions '1-MgO', '2-interface' and '3-Mg' with different colours in Fig. 6(a)), and the corresponding EELS elemental map of Mg. Some Mg K edge intensity is observed at the interface (position '2'), but at a level considerably lower than that in spectra '1' and '3' acquired from the regions inside MgO and Mg, respectively, suggesting a local depletion of Mg. The dissimilarity between the Mg K near edge structure in curves '2' and '1' excludes the

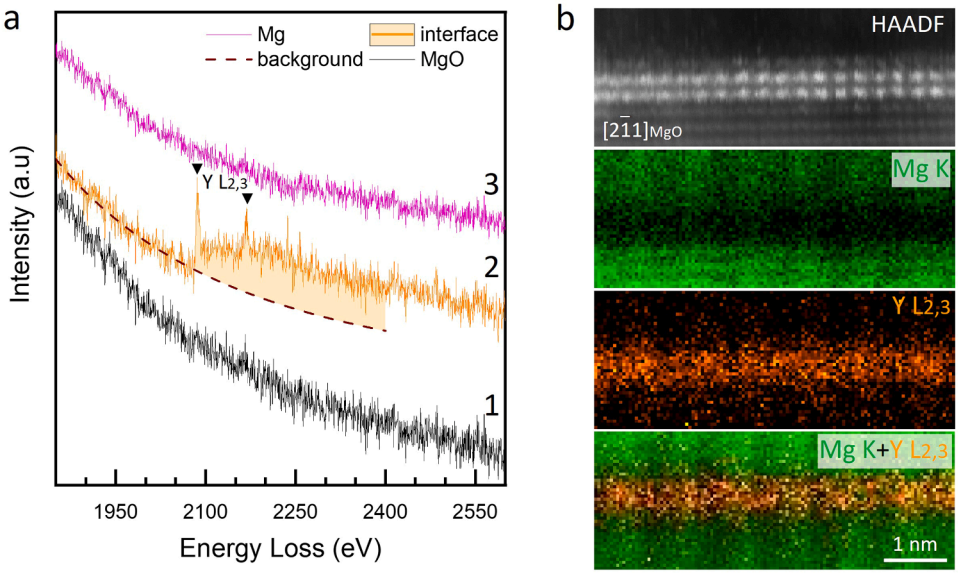

Fig. 3. Confirmation of Y segregation at the Mg/{111}$_{MgO}$ interface. (a) EELS spectra acquired from different positions across the Mg/{111}$_{MgO}$ interface in Mg-0.5Y: '1' (black) from the MgO particle, '2' (orange) from the interface, and '3' (pink) from the Mg matrix; and (b) HAADF STEM image and the corresponding EELS elemental maps of 'Mg' and 'Y' and 'Mg+Y' composite, confirming Y atoms concentrate in the interfacial layers at Mg/{111}$_{MgO}$ interface. Although the spectra in (a) are shown in 'arbitrary units' and vertically shifted for clarity, they are on the same vertical scale for intensity comparison.

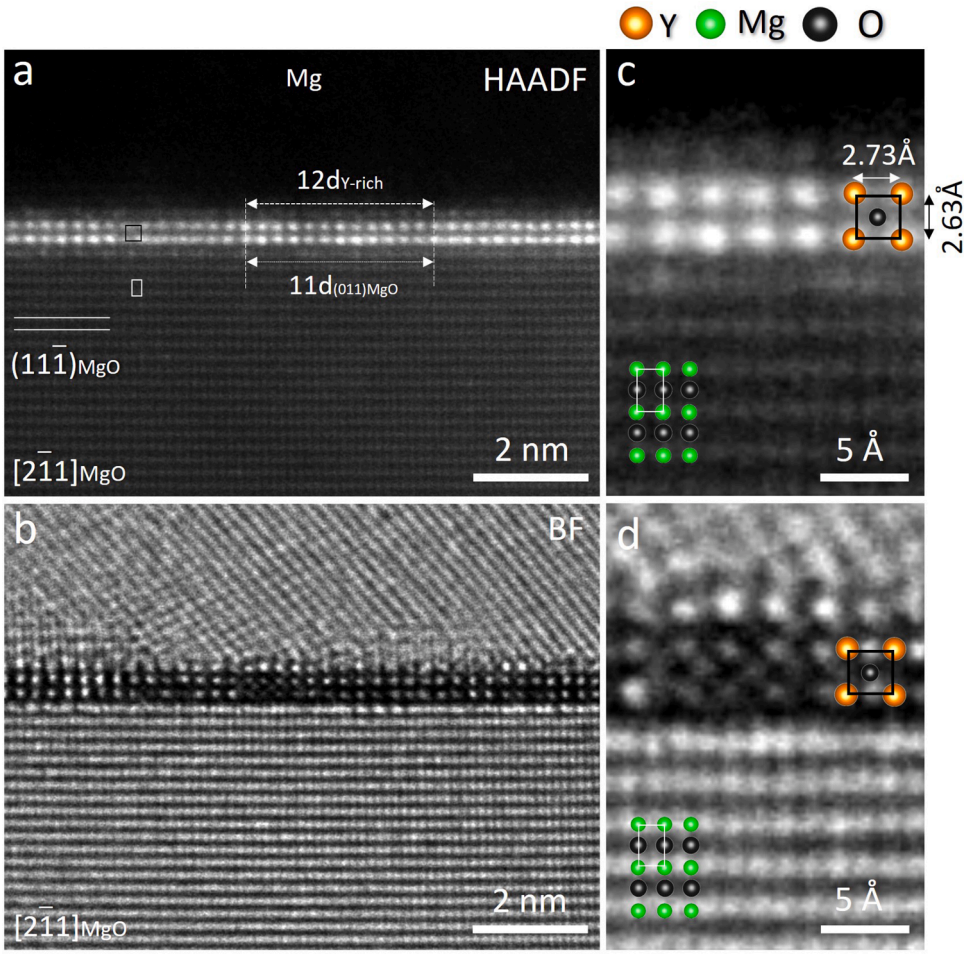

Fig. 4. Atomic-resolution (a, c) HAADF and (b, d) BF STEM images across an Mg/{111}$_{MgO}$ interface showing the atomic structure of Y-rich segregation layers at the interface in Mg-0.5Y. The incident beam was parallel to the $[2\bar{1}1]_{MgO}$ zone axis.

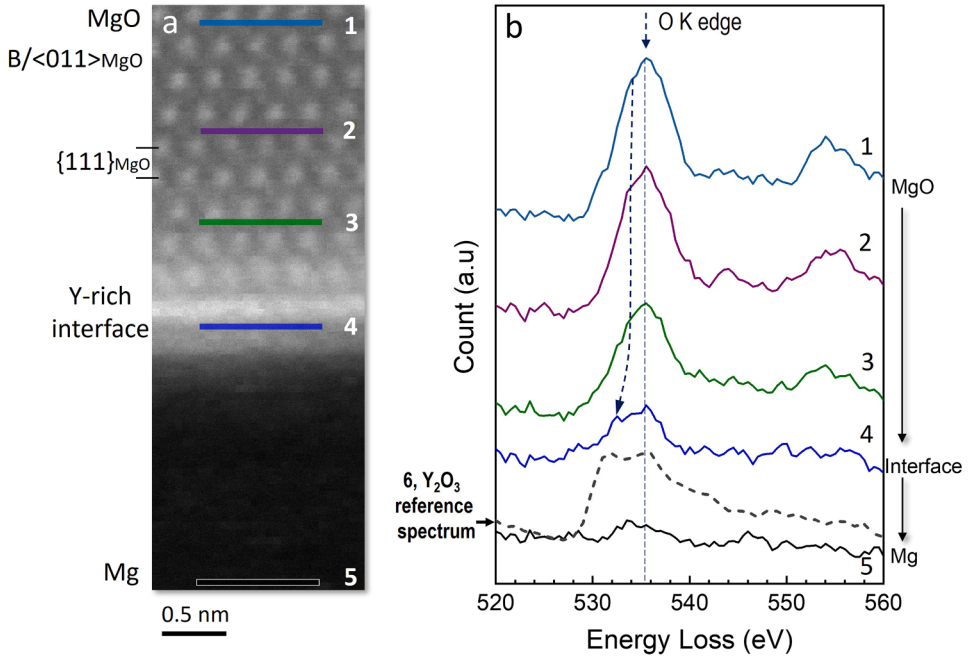

Fig. 5. Existence of O in the segregation layers confirmed by the energy-loss near edge-structure (ELNES) analysis of the O K edge across the Mg/{111}$_{MgO}$ interface in Mg-0.5Y, the incident electron beam was parallel to <011>$_{MgO}$. (a) Simultaneous HAADF image during EELS SI acquisition; and (b) EELS spectra extracted from five regions marked by different colours in (a) showing the evolution of ELNES of 'O' K edges across the Mg/{111}$_{MgO}$ interface with the Y-rich atomic layers. Although the spectra 1-5 in (b) are shown in 'arbitrary units' and vertically shifted for clarity, they are on the same vertical scale for intensity comparison.

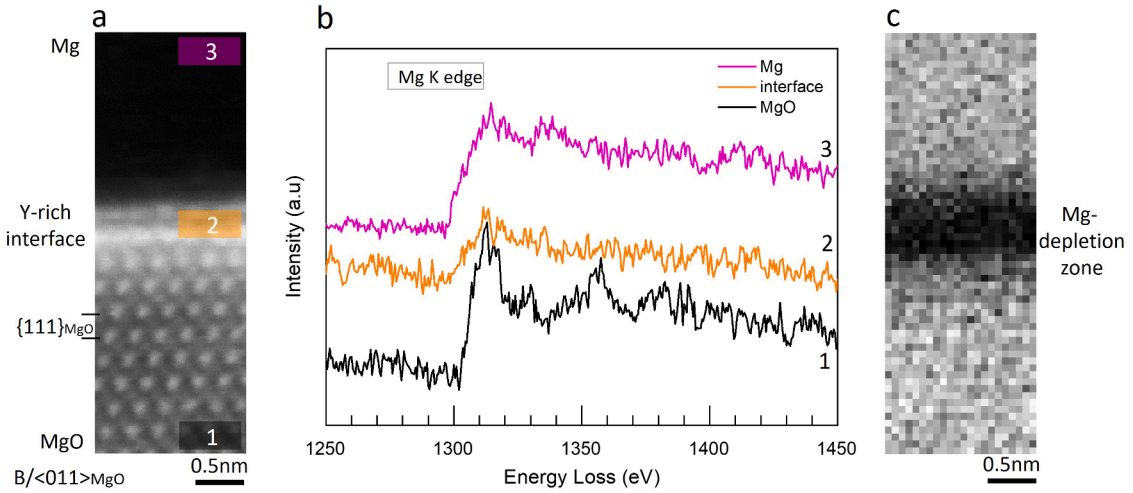

Fig. 6. Exclusion of Mg in the segregation layers confirmed by the ELNES analysis of the Mg K edge across the Mg/{111}$_{MgO}$ interface in Mg-0.5Y, the incident electron beam was parallel to <011>$_{MgO}$. (a) Simultaneous HAADF image during EELS SI acquisition; (b) EELS spectra extracted respectively from the marked ('1', black) MgO, ('2', orange) MgO/Mg interface and ('3', pink) Mg regions in (a); and (c) EELS elemental map showing the Mg depletion at the Mg/{111}$_{MgO}$ interface where Y atoms segregate. Although the spectra in (b) are shown in 'arbitrary units' and vertically shifted for clarity, they are on the same vertical scale for intensity comparison.

presence of Mg in the Y-rich segregation layer as Mg^{2+}. In contrast, a similarity in shape is seen between curves '2' and '3', suggesting that the residual Mg atoms detected in the interfacial region are metallic-like rather than ionic-bonded. In other words, Mg is absent in the Y-rich segregation layers (in the Mg^{2+} state), and the detected Mg signal at the interface by the EELS is mainly from the Mg matrix close to or overlapping with the segregation layers.

By now, we have identified structurally and chemically the similarity of the segregation layers to a reported FCC Y_2O_3 crystal [49]. A further HAADF STEM characterization of the Mg/{111}$_{MgO}$ interfaces in Fig. 7 from two perpendicular directions and one additional direction in-between provides confidence in these conclusions. As expected, the structure of the Y-rich segregation layers is different from the MgO matrix under all viewing directions. It is noted that the quasi-square pattern observed under the $[2\bar{1}1]_{MgO}$ zone axis (Fig. 7(a)) disappears and the Y-rich segregation layers become 'fuzzy' when the sample is rotated 30° to be viewed along the $[101]_{MgO}$ direction (Fig. 7(b)). When the structure is further rotated by 90° to the $[011]_{MgO}$ zone axis (Fig. 7 (c) and Fig. S5), the brighter atomic columns are resolved again, with the reappearance of the quasi-square pattern. The same pattern from the two perpendicular directions suggests that the symmetry of the Y-rich segregation layers, along its normal, is fourfold, which is different from the sixfold/threefold symmetry for the {111}$_{MgO}$ plane.

Therefore, the Y- and O-rich segregation layers can be identified as a two-dimensional compound (2DC) with a structure and composition similar to the reported FCC Y_2O_3 crystal [49], albeit with a slight variation in 'lattice constant'. Residual strains remain in Y_2O_3 2DC with respect to the strain-free bulk Y_2O_3 as the MgO/Y_2O_3 2DC with 11/12 matching does not fully accommodate the lattice misfit between Y_2O_3 2DC and MgO (Fig. 4). The orientation relationship (OR) between the MgO substrate and Y_2O_3 2DC is identified as OR1: $(11\bar{1})[011]_{MgO}//(100)[0\bar{1}0]_{Y2O32DC}$ (Fig. S6). A proposed 3-dimensional atomic configuration across the interface can be established accordingly (Fig. 8(a)). The model projections from $[011]_{MgO}$, $[101]_{MgO}$ and $[2\bar{1}1]_{MgO}$ directions are shown in Fig. 8(b-d), with the corresponding simulated HAADF images (by QSTEM package [46] and using parameters reflecting experimental conditions) presented in Fig. 8(e-g). Comparisons with the experimental HAADF STEM images (Fig. 7(a-c)) show excellent agreement, verifying the proposed structure and chemistry of the Y_2O_3 2DC segregation layers. After rotating 45° around the facet's normal, the quasi-square pattern changes to the expected lattice

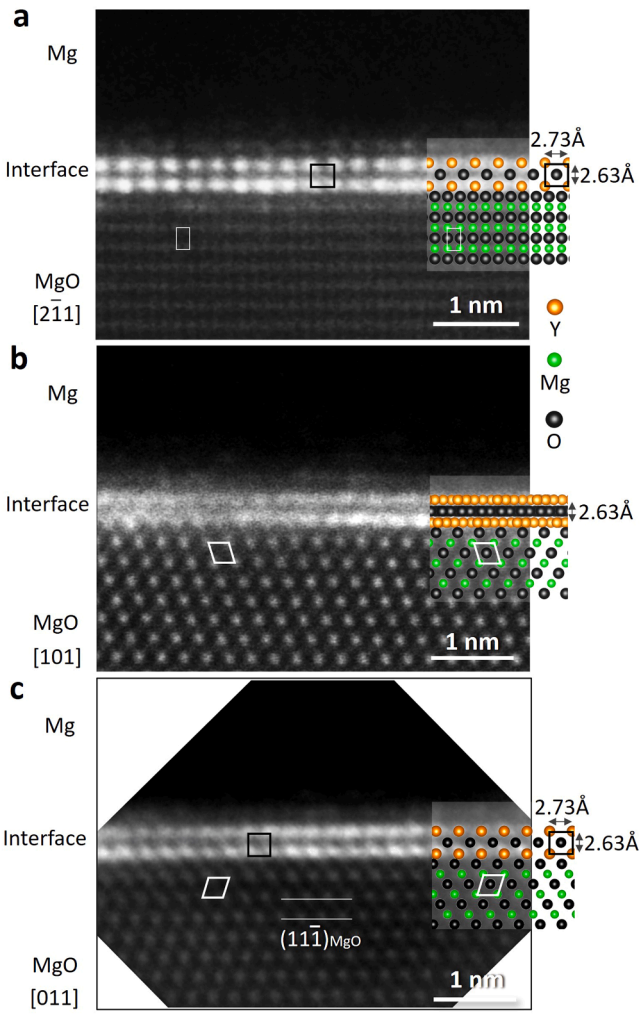

Fig. 7. Atomic structure of the Y-rich segregation layers at Mg/{111}$_{MgO}$ interface in Mg-0.5Y examined by atomic resolution HAADF STEM images from three different viewing directions. (a) $[2\bar{1}1]_{MgO}$; (b) $[101]_{MgO}$; and (c) $[011]_{MgO}$.

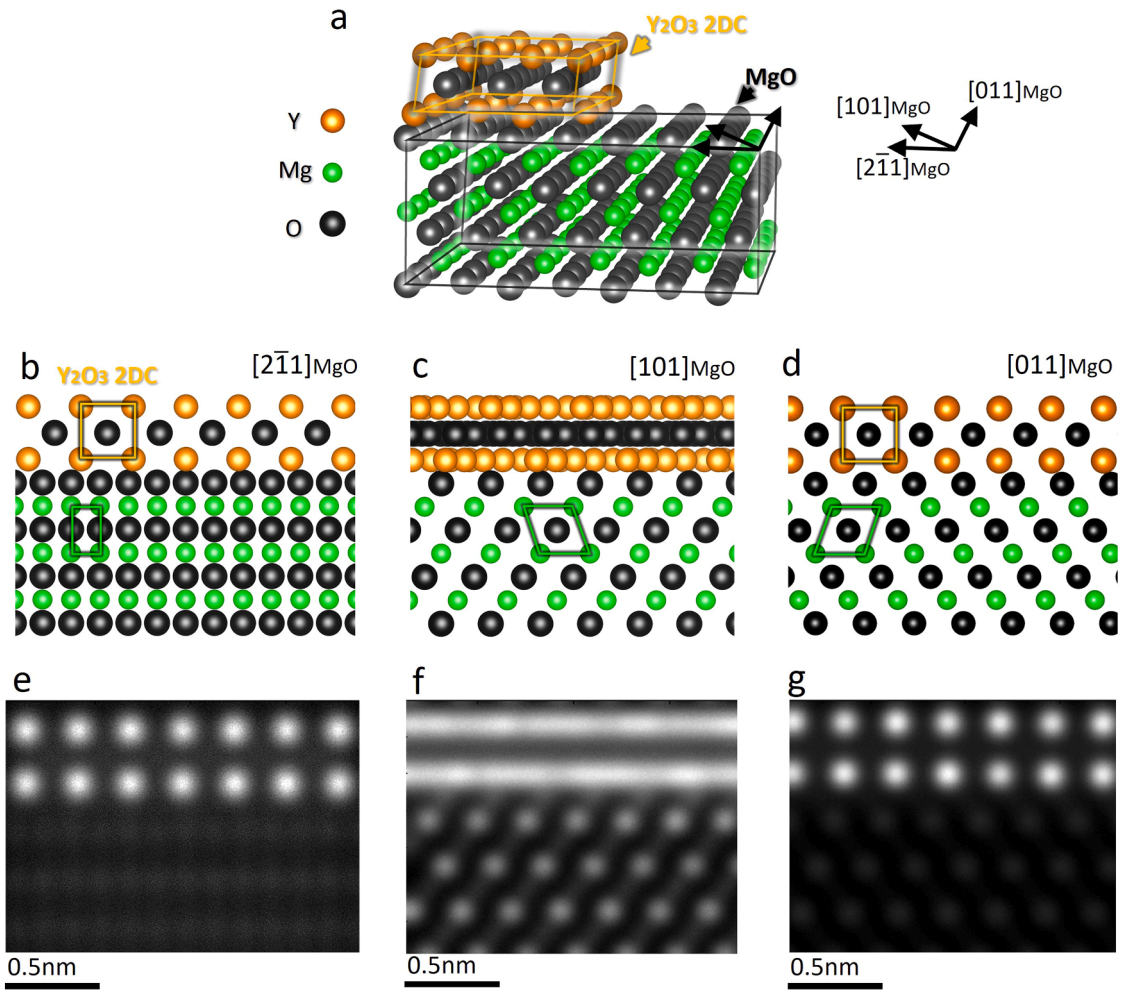

Fig. 8. (a) Three-dimensional illustration of the derived atomic model showing the Y_2O_3 2DC layers on top of the $(111)_{MgO}$ facet; (b-d) projections along (b) $[2\bar{1}1]$, (c) $[011]_{MgO}$, and (d) $[101]_{MgO}$ directions, respectively; and (e-g) the corresponding simulated STEM HAADF images using the QSTEM software package.

structure of Y_2O_3 2DC, as shown in Fig. S7. Moreover, the Y_2O_3 2DC at a single $Mg/(11\bar{1})_{MgO}$ interface was observed with simultaneously-acquired HAADF and iDPC STEM images from consecutive $[101]_{MgO}$, $[3\bar{1}2]_{MgO}$, $[21\bar{1}]_{MgO}$ projections within a 30° tilting range (Fig. S8). Despite the beam damage to the Y_2O_3 2DC during STEM observation at 300 kV, the quasi-square patterns of the Y-rich atomic columns can be recognized, in agreement with the atomic structure based on the proposed atomic model in this projection. Damage from the electron beam is likely also to affect the O atomic columns in the Y_2O_3 2DC, leading to a weakened-signal intensity and degraded periodicity.

3.4. *Segregation of Y at the Mg/{100}$_{MgO}$ interface*

Y segregation was also observed at the $Mg/\{100\}_{MgO}$ interface,

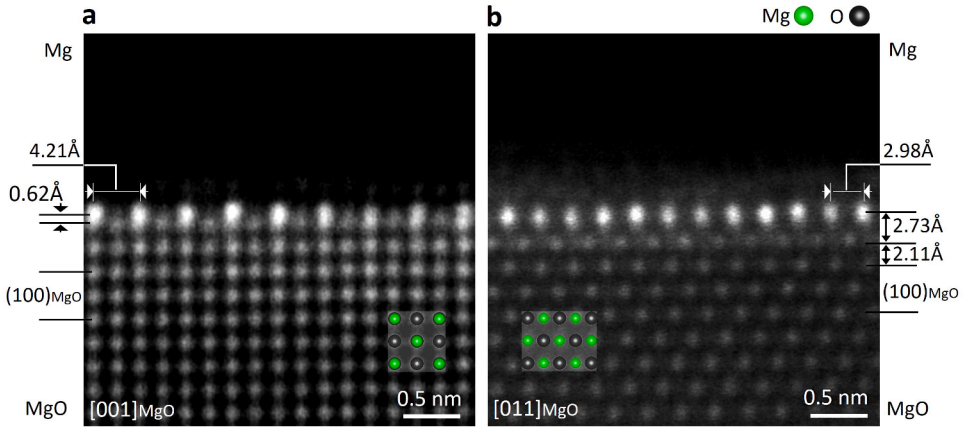

Fig. 9. Atomic structure of the Y-rich segregation layer at the $Mg/\{100\}_{MgO}$ interface in Mg-0.5Y examined by atomic resolution HAADF STEM images from two viewing directions. (a) $[001]_{MgO}$; and (b) $[011]_{MgO}$.

whose structure and chemistry are significantly different from those at the Mg/{111}$_{MgO}$ interface. The HAADF STEM images (Fig. 9) illustrate at the atomic scale how Y decorates the Mg/{100}$_{MgO}$ interface in Mg-0.5Y. The segregation of heavier Y atoms appears as atomic columns of higher brightness at the Mg/{100}$_{MgO}$ interface, being a monolayer coherent with the {100}$_{MgO}$ substrate. The monolayer presents an alternating dark-bright-dark pattern when observed along the [001]$_{MgO}$ zone axis (Fig. 9(a)), whereas for pure MgO each atomic column originally contains 50% Mg atoms and 50% O atoms to have equal intensity. This suggests a particular manner in which Y segregates to an Mg/{100}$_{MgO}$ interface. The separation of Mg and O columns, when viewed in the [011]$_{MgO}$ projection (Fig. 9(b)), helps identify that Y atoms occupy the Mg sites, where the interfacial monolayer's pattern appears as continuous brighter dots, whose positions nearly coincide with those expected of Mg columns in the MgO substrate, with minor displacements. More precisely, the Y-rich columns are elongated when observed in both zone axes, with a vertical protrusion of about 0.62±0.05 Å being identified with respect to the terminating (100)$_{MgO}$ plane. The elongated columns in the monolayer are attributed to the existence of Mg/O atoms (Fig. 9(a)) or Mg atoms (Fig. 9(b)) underneath and right in the original terminating (100)$_{MgO}$ plane. Therefore, Y atoms partially occupy specific terminating Mg atomic positions and vertically deviate from the Mg sites by 0.62 Å. The atomic resolution STEM/EDS maps in Fig. 10 show the chemical compositions across the Mg/{100}$_{MgO}$ interface under the

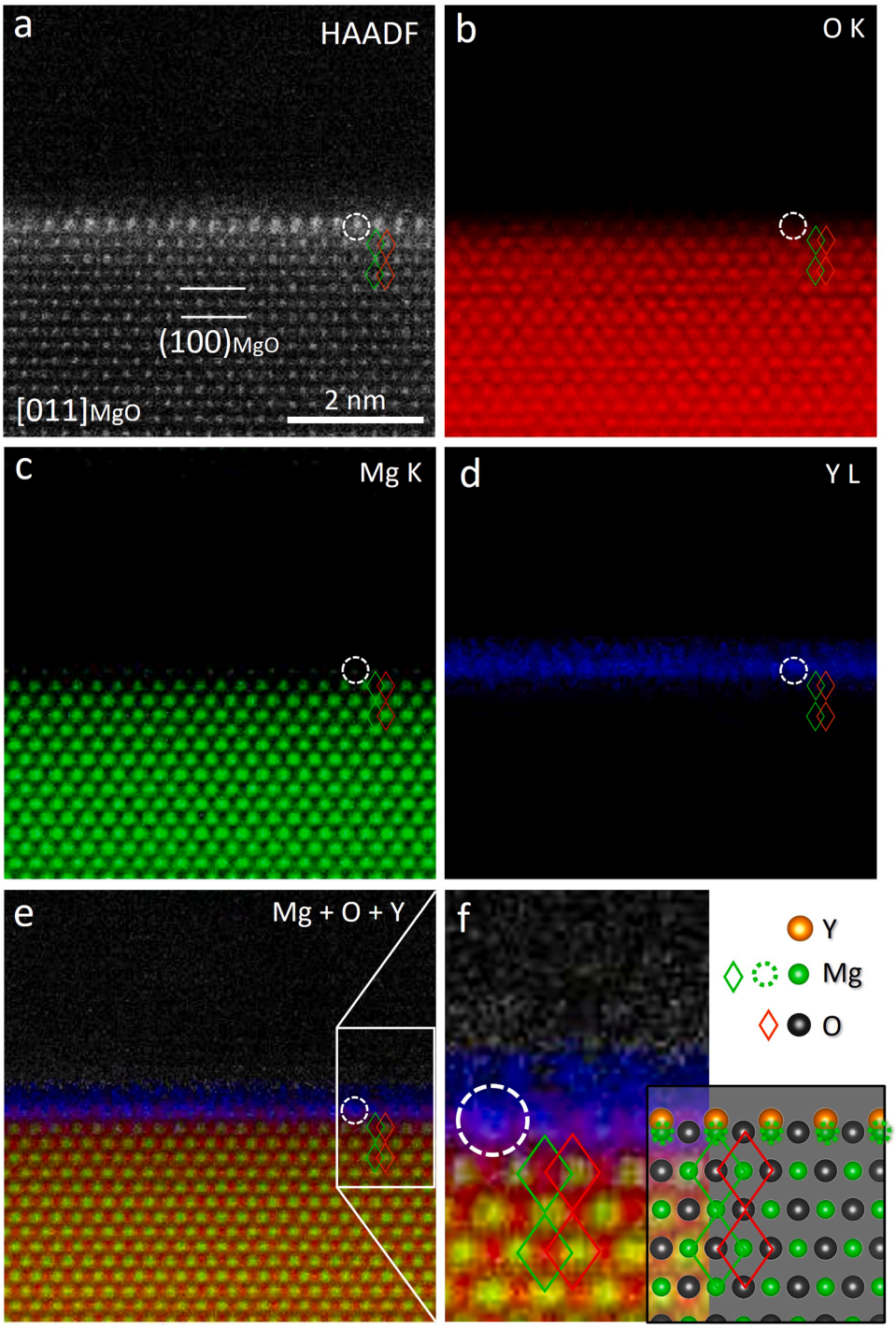

Fig. 10. STEM/EDS mapping showing the elemental distributions across the Mg/{100}$_{MgO}$ interface with the Y-rich monolayer, the incident beam was parallel to [011]$_{MgO}$. (a) HAADF STEM image; and (b-f) EDS elemental maps of (b) 'O'; (c) 'Mg'; (d) 'Y'; and (e) 'Mg+O+Y'. (f) Enlarged local areas on (e) with the superimposed atomic model. Green and red diamond marks represent the Mg and O lattices, respectively. The dashed green circles highlight the partial occupancy of Mg columns by segregated Y atoms at the interface.

$[011]_{MgO}$ zone axis. The Mg and O maps follow the atomic periodicity of MgO across the interface under this projection. It is identified that the Y-rich columns occupy the Mg sites in the terminating $(100)_{MgO}$ atomic plane. An example is highlighted by the dashed circles, where vertical protrusion of the Y-rich column is also noticed. The weak intensity of the remaining Mg atomic columns strongly suggests partial occupancy. Taken together, the HAADF STEM images and STEM/EDS results provide conclusive evidence that Y atoms selectively replace part of the terminating Mg atoms along with a slight geometric deviation perpendicular to the interface, likely due to the different ionic size of Y. Nevertheless, the Y occupation fraction in the interfacial monolayer remains to be determined.

The atomic configuration of the Y-rich monolayer at the Mg/$\{100\}_{MgO}$ interface is therefore established based on the above experimental observations. Fig. 11(a) and (b) compare the in-plane atomic arrangement of the Y-rich monolayer and the original $(100)_{MgO}$ plane, where Y atoms proportionally substitute the Mg atoms in a primitive square lattice pattern (a_{MgO}* a_{MgO}) marked by the dash green spheres (0 < y% < 100%), and offset 0.62 Å vertically. As projected along $[001]_{MgO}$ (Fig. 11(c)), every brighter and elongated atomic column of the monolayer contains y/2% Y (orange spheres), (50-y/2)% Mg (green dash spheres) and 50% O (black spheres) atoms, while every dark column of the monolayer contains 50% Mg (green spheres) and 50% O atoms; this is fully consistent with the observed periodic dark-bright-dark pattern (Fig. 9(a)). When viewed along $[011]_{MgO}$ direction (Fig. 11(d)), every brighter column in the monolayer contains y/2% Y atoms and (100-y/2)% Mg atoms. The monolayer presents as continuous brighter dots in HAADF STEM images (Fig. 9(b)) where O columns in between are almost invisible. The Y-rich monolayer therefore can be denoted as Mg(Y)-O 2DC, which is coherent to the $(100)_{MgO}$ facet as illustrated by the schematic in Fig. 11(e). Unfortunately, it was impossible to confirm local bonding through EELS spectrum imaging across the Mg/$\{100\}_{MgO}$ interface with Mg(Y)-O-2DC because of beam damage. Although a quantitative determination of the percentage of the Y in the interfacial monolayer is beyond the limit of the applied STEM-EELS or STEM-EDS in this work, HAADF image simulation was carried out to

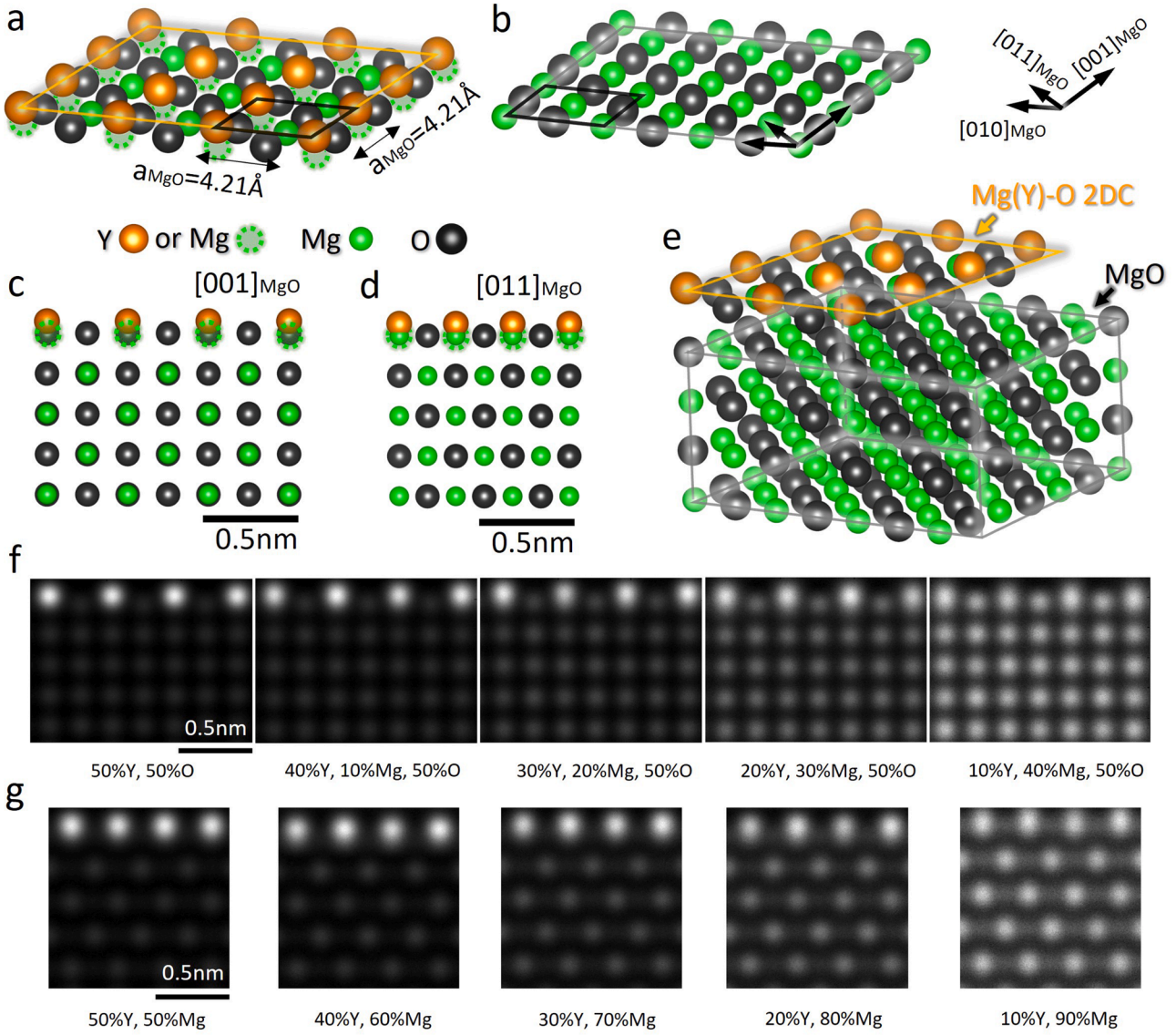

Fig. 11. (a) Atomic model of the termination of Mg(Y)-O 2DC monolayer, where y% Mg atoms with dash-circle marks in a (a_{MgO} *a_{MgO}) sublattice are replaced by Y atoms; (b) atomic model of the $(100)_{MgO}$ termination layer; (c-d) atomic configuration of Y, Mg and O atoms in the 2DC layer projected respectively along (c) $[001]_{MgO}$ and (d) $[011]_{MgO}$ directions; (e) three-dimensional illustration of the derived atomic model showing the segregation layers on top of the $(100)_{MgO}$ facet; and (g-h) simulated STEM HAADF images along the corresponding (f) $[001]_{MgO}$ and (g) $[011]_{MgO}$ directions using the QSTEM software package with varying number percentages of the Y atoms ($\frac{y}{2}$% from 10% to 50%) in the brighter atomic columns.

approximately estimate the composition of Y in the interfacial monolayer, as shown in Fig. 11(f) and (g). It is noticed that the brighter columns in the simulated images start having a vertical elongation when y/2% ≤ 30%. Specifically, when y/2% = 20%-30%, the brightness ratios of the Y-rich columns to the Mg/O columns (Fig. 11(f)) and the Mg columns (Fig. 11(g)) are close to those in the experimental HAADF images. This suggests that each Y-rich column contains about 20-30% Y, 30-20% Mg, and 50% O under the $[001]_{MgO}$ projection, while it contains about 20-30% Y atoms and 80-70% Mg atoms when viewed along the $[011]_{MgO}$ direction.

3.5. Native Y-decorated MgO particles enhance grain refinement

The employment of HSMC to the CP Mg melt disperses native MgO particles and promotes a certain level of CET and grain refinement. As shown in Fig. 12(a) and (b), fine and equiaxed grains are seen in the central region of the CPMg-HSMC-TP-1 ingot. The average grain size is 235.4±18.1 μm. After the addition of 0.5Y, further grain refinement is achieved in Mg-0.5Y-HSMC-TP-1 (Fig. 12(c) and (d)), where the grain structure is much finer and more uniform across the TP-1 ingot, with an average grain size of 105.5±4.3 μm. The grain size reduction is majorly attributed to the dispersity of Y-modified native MgO particles, in addition to a minor contribution from the weak growth restriction provided by 0.5Y, which only corresponds to a growth restriction factor Q=0.85 K. The grain structure is not homogeneous across the TP-1 ingot, due to expected differences in cooling conditions from the mould wall to the mould centre during the TP-1 casting. In the region with coarser grain size, constitutional undercooling is suppressed due to the slow atomic diffusion under a specific fast cooling rate [52]. The existing grains grow rapidly during this delay period to a large size, and release latent heat to cause recalescence that ceases further nucleation events. Such a necklace pattern can be mitigated by solutes with high diffusivity or increased growth restriction. In contrast, the lack of a sufficient number of nucleating substrates and adequate growth restriction causes a columnar and coarse grain structure in CPMg-TP-1 without HSMC treatment (Fig. S12(a) and (b)). Modification of native MgO particles in poor dispersity barely affects the grain size. The addition of 0.5Y does not achieve the columnar-to-equiaxed transition (CET) in Mg-0.5Y-TP-1, whose grain structure remains columnar with grains of large size (Fig. S12(c) and (d)). The quantified average width of the columnar grains is 816 ± 95.9 μm and 718.6 ± 225.9 μm for CPMg-TP-1 and Mg-0.5Y-TP-1, respectively.

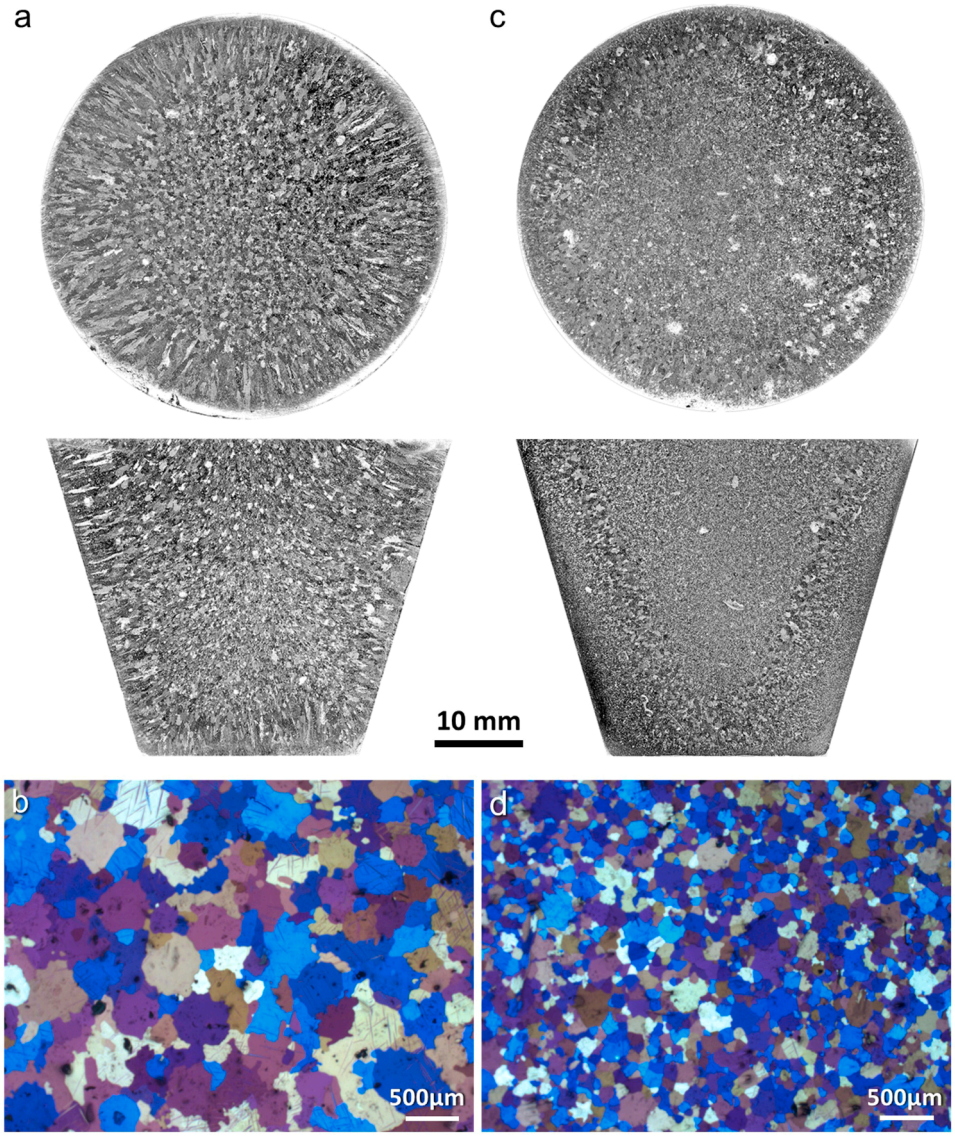

Fig. 12. Optical micrographs showing grain refinement improved by dispersed native MgO particles with modifications by the segregation of Y. (a-b) CP Mg-HSMC, 235.4±18.1 μm; and (c-d) Mg-0.5Y-HSMC, 105.5±4.3 μm. Both melts were treated by high shear melt conditioning before casting into TP-1 mould.

4. Discussion

4.1. Formation mechanism of 2DCs at the liquid-Mg/MgO interface

Elemental segregation is a general phenomenon occurring at various interfaces driven by the reduction of the total Gibbs free energy of the system [20,45]. It has been widely observed at the melt/substrate interfaces in various Al- and Mg alloys containing different inoculant particles [9,13,14,25,27]. This study provides for the first time experimental observations, analyses, and identifications of the formation of Y-segregation 2DCs at the Mg/MgO interfaces in a solidified Mg-0.5Y sample. However, the question remains whether their formations occur above liquidus or during the cooling of solid.

A process of elimination helps to reach a likely conclusion. As one of the generic complexion transitions appearing at general interfaces, elemental segregation appears as abrupt changes in structure or/and chemistry that are usually accompanied by discontinuous changes in macroscopic properties [53–55]. Similarly, the potency modification after elemental segregation generally affects the grain refinement behaviour of metallic materials [13,25,26]. The grain size will not change if the Y-segregation 2DCs form in the solid state during cooling, which contradicts our experimental results in Fig. 12 and Fig. S12. Moreover, if the segregation of Y occurs in the solid state, it is expected to have different types of complexions as a function of the geometric configurations of interfaces. It has been reported that monolayer, bilayer, trilayer or even nano-sized layers can form depending on the misorientation of grain boundary [54,56]. It also conflicts with experimental observations that there is only a unique type of Y-rich 2DC at each type of the Mg/MgO interface. Therefore, it is less likely that Y-segregation 2DCs form in the solid state. It sounds promising that the segregation of Y occurs in the Mg-0.5Y melt, forming specifically Y_2O_3 2DC at the liquid-Mg/$\{111\}_{MgO}$ interface and Mg(Y)-O 2DC monolayer at the liquid-Mg/$\{100\}_{MgO}$ interface, which changes the nucleation potency of native MgO particles as well as the as-cast grain size.

An extension of the Gibbs adsorption Isotherm has been recently proposed to quantitatively describe the interfacial segregation of solute in a dilute alloy melt [57]. The equation (25) in Ref. [57] suggests that interfacial segregation is favoured by i) a negative difference in interfacial energies approximated by $\Delta\gamma = \gamma^i_{Y(L)/MgO} - \gamma^i_{Mg(L)/MgO}$ in this case, ii) a positive interaction term Ω of a regular solution between solvent and solute atoms related to a positive enthalpy of mixing $\Delta_{mix}H^{Liquid}_{Mg-Y}$, and (iii) a positive difference in entropies of fusion between pure solvent and solute $\Delta S^i = \Delta_{fus}S_{Mg} - \Delta_{fus}S_Y$ [57].

A strong attractive interaction among Mg and Y in the liquid solution is proven to exist from a comprehensive CALHAD assessment of that binary system [58] and the following data is calculated from these thermodynamic parameters using the Pandat software [59]. A large negative value of the mixing enthalpy with the minimum value of $\Delta_{mix}H^{Liquid}_{Mg-Y} = -10.6$ kJ/mol at 41 at.% Y is obtained from the subregular solution [58]. The approximation by a regular solution equation to fit the dilute, Mg-rich range results in $\Delta_{mix}H^{Liquid.reg}_{Mg-Y} = -14$ kJ/mol at 50 at. % Y, corresponding to the interaction term Ω = -56 kJ/mol. This strong negative term impedes the interfacial segregation of Y. The coordination numbers $Z_l = 9$, $Z_V = 12$, $Z = 13$, in the notation of Ref. [57], are used for the numerical calculations. Although the value of the entropy difference, $\Delta S^i = 2.837$ J/mol/K calculated from Ref. [58], is positive it only accounts for a small promotive contribution to the interfacial segregation of Y. At 700°C its contribution is about 18 times smaller compared to the impeding Ω term. The remaining impeding effect can be cancelled if the value of $\Delta\gamma$ is negatively large enough. The interfacial energies of pure liquid elements and MgO are not known. However, the difference $\Delta\gamma$ can be predicted by solving equation (25) in Ref. [57] with the data given above. At 700°C the limit is $\Delta\gamma < -1.05$ J/m^2 to result in enrichment of Y. The value of $\Delta\gamma = -1.39$ J/m^2 is obtained for reasonable atomic segregation of factor 10 with 1.137 at.% Y (4.0 wt.% Y) at the Liquid/$\{111\}_{MgO}$ interface from the bulk Mg-0.5Y (0.137 at.% Y) melt. The value may not be quantitatively precise as it depends on the accuracy of input data and assumptions in the model, where $\Delta\gamma$ stands for the liquid component difference. However, it may qualitatively indicate that the segregation of Y solute atoms to the liquid-Mg/MgO interface should give rise to the reduction of interfacial energy.

The thermodynamic conditions for the formation of bulk Y_2O_3 particles, which were rarely observed in Mg-0.5Y, are revealed by the isothermal section at 700°C and ambient pressure of the equilibrium phase diagram for the Mg-Y-O ternary system (Fig. 13). It is calculated using Pandat and the PanMg database [60]. The magnified Mg-rich part in Fig. 13(b) shows that the bulk Mg-0.5Y liquid alloy is saturated at 0.24 wt.% O with MgO. This small oxygen content is readily picked up from the ambient during melting because of the extremely low partial pressure of O_2, $p(O_2) = 4.9\bullet10^{-54}$ bar, calculated at the tie line Liquid+MgO. Therefore, MgO is the only stable native oxide in that alloy which is also observed experimentally. More than 3.9 wt.% Y in the liquid alloy is required to expect Y_2O_3 as the stable bulk oxide. It is interesting to note that under the assumed segregation of factor 10 with 4.0 wt.% Y in the liquid monolayer at the Liquid/$\{111\}_{MgO}$ interface one could obtain a local three-phase equilibrium with Y_2O_3 at that interface. Y could be an active segregating element as its segregation tendency can be found in other systems, where the phenomena could be simply understood as driven by the reduction of surface/interface/grain-boundary free energy [61–63]. On the contrary, the atomistic mechanism varies. For instance, the large work of adhesion of Y to the MgO {111} surface results from the band filling modification and orbital hybridization [61]. The strong Y-O bonds of partial covalent characteristics were also attributed to the segregation of Y that stabilises the Σ31 grain boundary of alumina [62]. In the Mg-Y alloy, the segregation of Y at grain boundaries is driven by both the atomic size misfit and the synergetic interaction between Y and impurity Ni [63].

4.1.1. Y_2O_3 2DC at the Mg/$\{111\}_{MgO}$ interface

The terminating $\{111\}_{MgO}$ is a polar facet that is screened by the surrounding Mg matrix, where the terminating Mg atoms only have three 'Mg-O' bonds to the O atoms beneath. As a result, they are under-coordinated compared to the ones inside with six bonds. In the Mg-0.5Y melt, the segregation of Y gradually builds up excess Y atoms at the interface and reduces the interfacial energy. Once the composition reaches a critical value, the weakly-bonded terminating Mg atoms ($\{111\}_{Mg(MgO)}$) are replaced by the Y atoms that form stronger but longer bonds to the oxygen atoms beneath ($\{111\}_{O(MgO)}$) [49,50,64]. If a Y monolayer forms epitaxially on the original $\{111\}_{Mg(MgO)}$ site, it would be unstable due to the longer 'Y-O' bond length than 'Mg-O' (2.28 Å [49] vs. 2.11 Å [50]), the differences in valence state (Y^{3+} vs. Mg^{2+}), and atomic size ($R_Y = 2.12$ Å vs. $R_{Mg} = 1.45$ Å [65]). The interfacial Y atoms, therefore, have to locally readjust together with O atoms, forming a Y_2O_3 2DC with a different structure from MgO under the identified OR1 (Fig. 8) to stabilize the interfacial structure. Furthermore, the thermodynamic criterion in Fig. 13 and the absence of driving force from interfacial energy reduction for Y segregation towards a Y_2O_3 interface together prevent the Y_2O_3 2DC from thickening and rule out the further growth or even the formation of a bulk Y_2O_3 phase.

4.1.2. Mg(Y)-O 2DC monolayer at the Mg/$\{100\}_{MgO}$ interface

The terminating $\{100\}_{MgO}$ is non-polar, containing 50% Mg and 50% O atoms that share the same face-centred sublattice with a translating shift of $\frac{1}{2}$ <100>$_{MgO}$ from each other (Fig. 11(b)). The substitution of these Mg atoms is relatively more difficult than that at the Mg/$\{111\}_{MgO}$ interface since each terminating Mg atom is bonded by five surrounding O atoms (just slightly under-coordinated). Similarly, due to the differences in bond length, valence state, atomic size, and the repulsive coulomb force, the whole replacement of $\{100\}_{Mg(MgO)}$ by Y will add

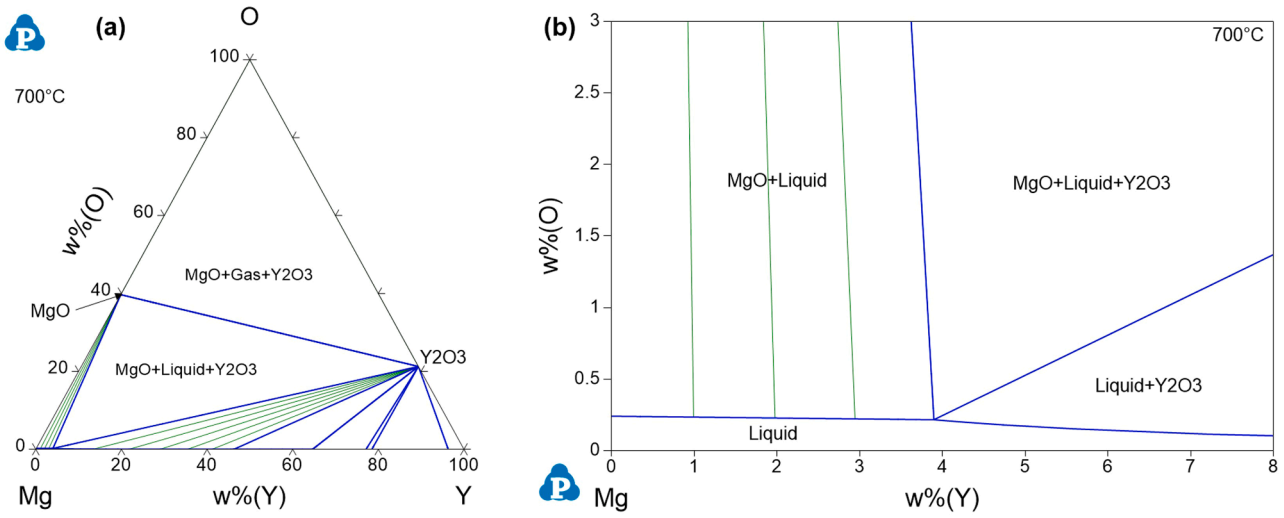

Fig. 13. Isothermal section at 700°C of the equilibrium phase diagram of Mg-Y-O ternary system calculated by Pandat and PanMg with (a) complete composition range and (b) Mg-rich corner with Y content up to 8 wt.%.

more energy penalty to the system; only part of them in the terminating layer can be substituted. The proportional substitutions of the (a_{MgO}*a_{MgO}) Mg sublattice (Fig. 11(a)) by Y atoms ensure the Y-Y spacings and a balance between the system's total free energy and the charge penalty. Owing to the larger bond length, the substituting Y atoms are not stable at the original Mg sites, the accommodation requires a vertical offset 0.62 Å (Fig. 9 and Fig. 10), which increases the Y-O distance to 2.2 Å (closer to 2.28 Å in Y_2O_3 [49]). This is in analogy to the case where segregated Y atoms energetically prefer expanded positions along a Σ31 grain boundary of alumina [62]. In the meantime, the formation of Mg vacancies could be a way to maintain charge neutrality. Vacancy defects could cause local strain fields that add more contrast to the coherent Mg(Y)-O 2DC under the MAADF STEM mode (Fig. 2(b) and (e)).

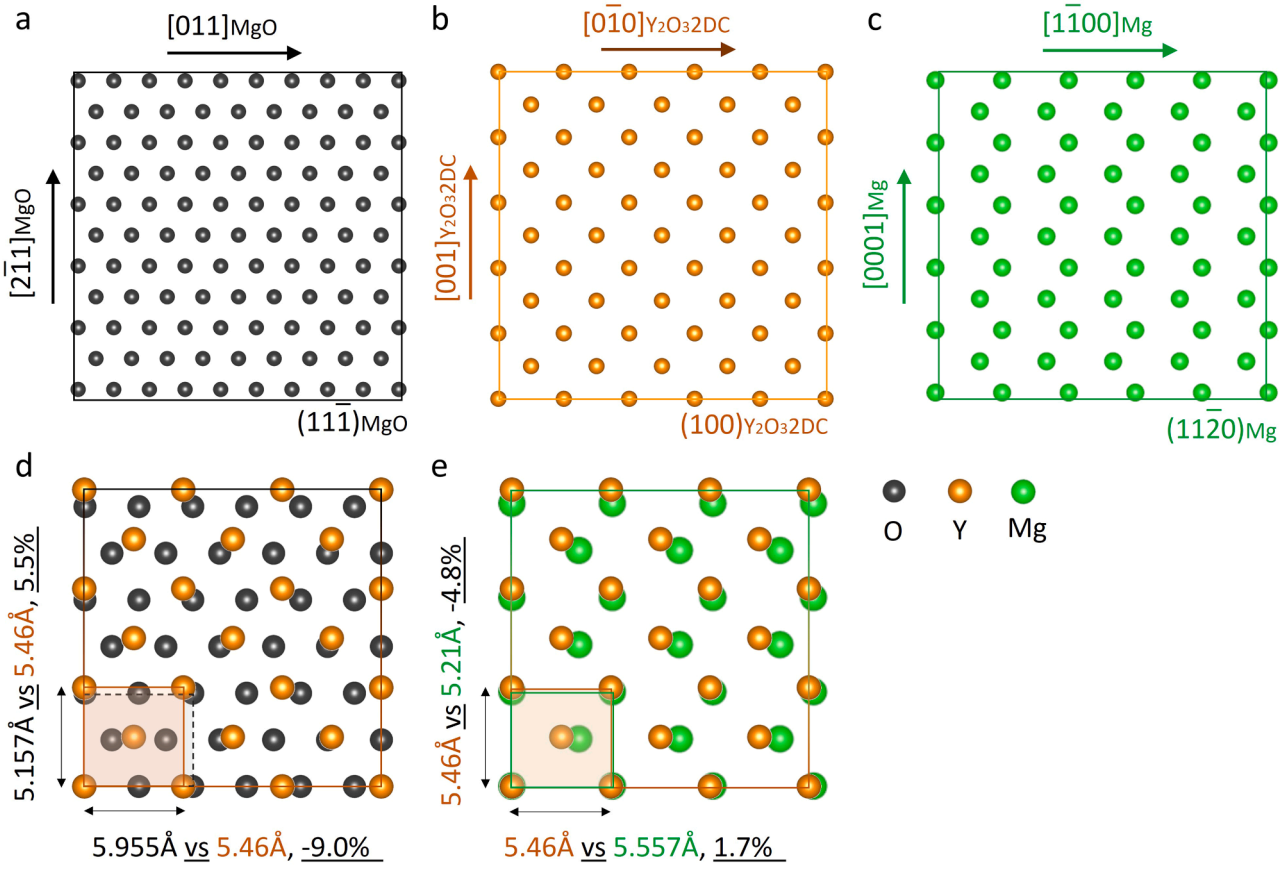

Fig. 14. Schematics showing the atomic matching between the Y_2O_3 2DC-decorated {111} MgO particle and Mg matrix under certain orientation relationships. (a-c) The atomic configurations of the matching planes of (a) $(11\bar{1})_{MgO}$, (b) $(100)_{Y2O32DC}$ and (c) $(11\bar{2}0)_{Mg}$; (d-e) overlapping atomic configuration and lattice misfit measurements based on (d) OR1: $(11\bar{1})[011]_{MgO}$ // $(100)[0\bar{1}0]_{Y2O32DC}$ and (e) OR2: $(100)[0\bar{1}0]_{Y2O32DC}$ // $(11\bar{2}0)[1\bar{1}00]_{Mg}$.

4.2. Nucleation potency manipulated by Y-segregation 2DCs

Y-segregation 2DCs modify native MgO particles and act as new substrates for nucleating αMg. Their structure and composition, which are different from the original terminating facets, cause variations in nucleation potency.

4.2.1. Y_2O_3 2DC enhances nucleation potency of {111} MgO

A good crystallographic match between two phases at the interface is widely accepted as a prerequisite for a low-energy configuration. Therefore, the lattice misfit at the interface between a solid phase and a substrate is one of the important factors determining the substrate's nucleation potency [2,7,8,66]. The {111} MgO was considered a relatively impotent substrate to nucleate αMg due to the relatively large lattice misfit of 7.9 % under the orientation relationship of (111)$[01\bar{1}]_{MgO}$//(0002)$[11\bar{2}0]_{Mg}$ [30]. As illustrated by the atomic matching under certain ORs in Fig. 14, the Y_2O_3 2DC formed on a {111} MgO substrate, acting as an intermediate, significantly reduces the misfit value to 1.7 %, hence rendering the modified {111} MgO more potent for nucleating αMg. There is a semi-coherent interface between {111} MgO and Y_2O_3 2DC under the observed OR1, with the calculated lattice misfits being 5.6 % and -9.0 % along $[2\bar{1}1]_{MgO}$//$[001]_{Y2O32DC}$ and $[011]_{MgO}$//$[0\bar{1}0]_{Y2O32DC}$ directions, respectively. The intermediate Y_2O_3 2DC achieves a minimum misfit with the αMg under OR2: (100)$[0\bar{1}0]_{Y2O32DC}$//$(11\bar{2}0)[1\bar{1}00]_{Mg}$, being 1.7% along the direction of $[0\bar{1}0]_{Y2O32DC}$//$[1\bar{1}00]_{Mg}$. A similar OR had been experimentally observed between the nucleated Mg crystalline flakes and micron-sized BCC Y_2O_3 particles in an Mg77Cu12Y6Zn5 metallic glass system, which is (040)$[100]_{B\text{-}Y2O3}$//$(1\bar{2}10)[1\bar{1}00]_{Mg}$ [67]. Furthermore, we reidentify the phase at the intermediate zone between Mg flakes and BCC Y_2O_3 as FCC Y_2O_3 rather than Cu after carefully reanalysing the HRTEM and STEM/EDS results in Ref. [67]. The intermediate FCC Y_2O_3 holds a cube-on-cube OR with BCC Y_2O_3, thus owning the same OR2 with the Mg flakes. The experimental validation of OR2 and the low lattice misfit accordingly verify that Y_2O_3 2DC is potent for nucleating αMg. In other words, the segregation of Y has manipulated {111} MgO into a substrate of better potency for the nucleation of αMg.

In addition to the structural considerations, previous work has suggested that chemistry also plays an important role in determining the potency of a substrate [10–14]. By attracting liquid atoms for pre-nucleation above liquidus, the presence of 'attractive' elements promotes the subsequent heterogeneous nucleation [11]. The concept of 'attractiveness' can be evaluated by the regular mixing enthalpy between two element atoms in the liquid phase. According to our results, Y atoms of Y_2O_3 2DC serve as the element in direct contact with the liquid Mg atoms (Fig. 4 and Fig. S8). The regular mixing enthalpy between Y and Mg in the liquid, as calculated above, is $\Delta_{mix}H^{Liquid,reg}_{Mg-Y} = -14$ kJ /mol, suggesting a strong attractive force between Y and Mg atoms, which leads to a promotion of prenucleation resulting in enhancements of both atomic layering and in-plane ordering. The following heterogeneous nucleation will be promoted as well since the end state of prenucleation serves as the starting point for heterogeneous nucleation.

4.2.2. Mg(Y)-O 2DC reduces nucleation potency of {100} MgO

With a lattice misfit of 7.9 % to αMg based on the observed OR, cubic {100} MgO was also treated as a relatively impotent substrate [30]. In addition, the nucleation potency deteriorates further as the terminating $\{100\}_{MgO}$ planes are atomically rough as a result of the different chemical affinities of terminating O^{2-} and Mg^{2+} ions to the liquid Mg atoms [12].

After the addition of 0.5Y, the newly formed Y-containing monolayer, *i.e.* the Mg(Y)-O 2DC, coherently matches the $\{100\}_{MgO}$ plane, therefore does not alter the original lattice misfit between the MgO and solid Mg. However, the vertical protrusion by 0.62 Å of the Y atoms (Fig. 9 and Fig. 10) introduces extra atomic roughness to the 2DC layer, which expectedly impedes the prenucleation [17] and thus leads to the decrease of the {100} MgO particles' nucleation potency. This may outweigh the positive factor of attractiveness between liquid Mg and terminated Y atoms. Furthermore, there are various types of chemical bonds between the Y, Mg and O atoms in the 2DC layer, and such complex configuration of chemical bonds may interfere with the atomic ordering of the liquid Mg atoms close to the interface. This further impedes the prenucleation behaviour; the poorly ordered crystalline Mg atomic layers act as a poor precursor for subsequent nucleation. As a result, the formation of the atomically rough Mg(Y)-O 2DC at the Mg/$\{100\}_{MgO}$ interface would decrease the nucleation potency of cubic {100} MgO particles, despite an unchanged lattice misfit.

4.3. Grain refining mechanism in Mg-0.5Y-HSMC

The grain size after solidification is determined by the number density of nuclei that are able to freely grow before recalescence; nucleant particle's potency, number density and solutes are critical for grain refinement. Without sufficient potent particles and growth restriction, the solidified Mg-0.5Y is comprised of columnar grains of large width (Fig. S12(c) and (d)). Solidification with sufficient particles but insufficient solutes causes fine columnar grains, such as the near-mould parts of CP Mg-HSMC shown in Fig. 12(a) and (b).

In Mg-0.5Y-HSMC, the addition of 0.5Y and the application of HSMC synergistically lead to a couple of positive effects on grain refinement. Firstly, the formation of Y_2O_3 2DC manipulates the relatively impotent {111} MgO particles into potent substrates. Although the Mg(Y)-O 2DC further degrades the potency of {100} MgO particles and the possible truncated {100} facets on {111} MgO particles, they do not disturb the grain refinement as a consequence of nucleation competition [7]. Moreover, since {111} MgO particles account for the major component of native MgO, there are sufficient potent particles even after the loss of impotent {100} MgO particles. Secondly, HSMC accelerates the process of Y segregation by stimulating mass transport in the Mg-0.5Y melt [25]. Meanwhile, Y segregation enhances the dispersion of native MgO particles during HSMC treatment by reducing interfacial energy [68]. Copious potent {111} MgO particles with Y_2O_3 2DC are therefore created in the melt of Mg-0.5Y-HSMC. Lastly, 0.5Y also provides sufficient growth restriction to enable more potent {111} MgO particles to participate in nucleation and grain initiation before recalescence, eventually causing the CET and grain refinement.

In summary, the grain refining mechanism in Mg-0.5Y-HSMC can be attributed to the enhanced potency of {111} MgO particles with Y_2O_3 2DC modification, their dispersity and abundant number density, and the sufficient growth restriction provided by 0.5Y.

4.4. Atomic engineering of nucleant substrate through elemental segregation

The compatibility of atomic configuration and chemistry at the interface between a nucleant substrate and the nucleated solid determines how potent the substrate is. Once the added alloying elements segregate to the metal/substrate interface, the structural and chemical state of the terminating surface is modified; its nucleation potency is thus altered accordingly. This experimental work has demonstrated conclusively that Y segregation can atomically engineer the native MgO's potency through the formation of Y-rich 2DCs. Specifically, the Y_2O_3 2DC reduces the lattice misfit with Mg solid down to 1.7 % and has chemical attractiveness to the liquid Mg atoms, rendering the {111} MgO particles more potent substrates. In contrast, the Mg(Y)-O 2DC degrades further the relatively impotent {100} MgO by introducing atomic-level surface roughness.

Our experimental observations of Y segregation at Mg/MgO interfaces add to the already wide body of research about interfacial segregation [4,9,10,13,14,21,25,27], demonstrating that atomic engineering of metal/substrate interfaces could be a common phenomenon

of critical importance in understanding the solidification process and designing desired microstructure. For example, it has been widely accepted that the potency variation of TiB_2 substrates through the segregation of Ti, Zr, or Si determines the final grain size of the inoculated Al alloys. Besides, minor additions of Ca and Zr cause significant grain refinement respectively in Mg-Ca [36] and Mg-Zr [21] alloys with HSMC treatment, with further solute additions (Zr < 0.3 %) affecting marginally the grain size. It has been demonstrated that the grain refinement was attributed to the large numbers of native MgO particles whose surfaces have been modified by the interfacial segregation of Ca or Zr.

Atomic engineering through elemental segregation has added an extra variable in a solidification process, which not only explains the grain refining behaviours in the literature but also offers a strategy to take full advantage of either the endogenous or exogenous nucleant particles in the melt for grain refinement. According to the configuration of nucleant particles in a melt, the performance can be enhanced by either impeding or promoting nucleation through atomic engineering. Practically, the external addition of grain refiners with particles of higher potency than native impurity particles is the traditional approach to promote heterogeneous nucleation for grain refinement. In this case, maximization of their potency by interfacial segregation is applicable for optimal grain refinement. Concurrently, any interfacial segregations that poison the nucleant particles must be avoided to prevent nucleation competition. Otherwise, the low-number-density native particles take over to dominate the solidification process for coarse grain structure. In contrast, in the case where a certain type of native particle is already in sufficient number density and other types of impurity particles are in scarce quantity, impeding their capacity for heterogeneous nucleation has been demonstrated to be a new approach to more significant grain refinement. This is counterintuitive to the traditional wisdom of making nucleant particles more potent for grain refinement. According to the explosive grain initiation (EGI) scheme [34], the melt keeps cooling down until the thermal undercooling meets the criteria for both heterogeneous nucleation and grain initiation on a huge number of impotent particles, which nucleate and initiate grains almost simultaneously and cause an immediate recalescence. The grain refinement map suggests that the more impotent the nucleant particles are, the more significant grain refinement can be achieved based on the EGI scheme [34]. This implies that atomic engineering could offer a strategy to boost grain refinement in different circumstances.

5. Conclusions

1 The native MgO particles present as predominant inclusions in commercial purity (CP) Mg and Mg-0.5Y melts are either {111} or {100} faceted, with their morphology being truncated octahedral (octahedral) or cubic, respectively. The size of the particles is in the range of a few tens to hundreds of nanometers. The addition of 0.5 wt.% Y to CP-Mg melt does not result in any changes in the phase, morphology, size, and size distribution of the native MgO particles.

2 In Mg-0.5Y, the segregation of Y solute atoms occurs at both the Mg/$\{111\}_{MgO}$ and Mg/$\{100\}_{MgO}$ interfaces, leading to the formation of interfacial Y-rich 2-dimensional compounds (2DCs). The segregation behaviour of Y is greatly affected by atomic configurations of the terminating $\{111\}_{MgO}$ and $\{100\}_{MgO}$ surface, resulting in differences in structure and composition between the two Y-rich 2DCs.

3 The Y-rich 2DC at the Mg/$\{111\}_{MgO}$ interface is identified as Y_2O_3 2DC, whose structure and chemistry resemble two {200} atomic planes of an FCC Y_2O_3 phase. The orientation relationship between the MgO substrate and the Y_2O_3 2DC above is: $(11\bar{1})[011]_{MgO}$ // $(100)[0\bar{1}0]_{Y2O32DC}$.

4 The Y-rich 2DC at the Mg/$\{100\}_{MgO}$ interface is identified as an Mg (Y)-O 2DC monolayer coherently matching with the terminating $\{100\}_{MgO}$ substrate, whose formation is through the partial substitution of the terminating Mg atoms in an Mg sublattice (a_{MgO}*a_{MgO}) by Y atoms. But the Mg(Y)-O 2DC is atomically rough due to the vertical protrusion of Y atoms (0.62 Å) relative to the original $\{100\}_{MgO}$ plane.

5 After the addition of 0.5 wt.% Y and the application of high shear melt conditioning that promotes interfacial segregation and particle dispersity, the well-dispersed native MgO particles with Y modifications result in grain refinement in the Mg-0.5Y-HSMC TP-1 ingot.

6 As verified by extensive transmission electron microscopy work, atomic engineering of Mg/MgO interfaces is applicable through the segregation of Y.

Declaration of interests

The authors declare that they have no known competing financial interests or personal relationships that could have appeared to influence the work reported in this paper.

The authors declare the following financial interests/personal relationships which may be considered as potential competing interests:

Acknowledgements

EPSRC is gratefully acknowledged for financial support under grant number EP/N007638/1. The SuperSTEM Laboratory is the U.K National Research Facility for Advanced Electron Microscopy, supported by EPSRC under grant number EP/W021080/1. SHW gratefully acknowledges the China Scholarship Council (CSC) for financial support and ETC at Brunel University for providing access to the facilities. The authors would like to gratefully acknowledge Dr. Feng Wang, Dr. Jayesh Patel and Mr. Peter Lloyd for their assistance in casting experiments and the inspiring discussion, and Dr Feng Gao and Dr Hua Men for reviewing the manuscript and invaluable discussion. SHW is also extremely grateful to Dr. Demie Kepaptsoglou at SuperSTEM Laboratory for her assistance and expertise during the characterisation sessions. Special thanks go to Dr. Chamini Mendis for organizing demo sessions provided by JEOL Ltd. and Dr. Arno Meingast from ThermoFisher Scientific.

Supplementary materials

Supplementary material associated with this article can be found, in the online version, at doi:10.1016/j.actamat.2023.119147.

References

[1] A.L. Greer, Overview: Application of heterogeneous nucleation in grain-refining of metals, J. Chem. Phys. 145 (2016), 2111704.
[2] M.X. Zhang, P.M. Kelly, M. Qian, J.A. Taylor, Crystallography of grain refinement in Mg-Al based alloys, Acta Mater 53 (2005) 3261–3270.
[3] M. Volmer, A. Weber, Keimbildung in übersättigten Gebilden, Zeitschrift Für Phys. Chemie. 1 (1926) 277–301.
[4] W.T. Kim, B. Cantor, An adsorption model of the heterogeneous nucleation of solidification, Acta Metall. Mater. 42 (1994) 3115–3127.
[5] J.C. Fisher, J.H. Hollomon, D. Turnbull, Nucleation, J. Appl. Phys. 19 (1948) 775–784.
[6] T.E. Quested, A.L. Greer, Athermal heterogeneous nucleation of solidification, Acta Mater 53 (2005) 2683–2692.
[7] Z. Fan, An epitaxial model for heterogeneous nucleation on potent substrates, Metall. Mater. Trans. A. 44 (2013) 1409–1418.
[8] D. Turnbull, B. Vonnegut, Nucleation Catalysis, Ind. Eng. Chem. 44 (1952) 1292–1298.
[9] L. Wang, W. Lu, Q. Hu, M. Xia, Y. Wang, J. Li, Interfacial tuning for the nucleation of liquid AlCu alloy, Acta Mater 139 (2017) 75–85.
[10] B. Cantor, Heterogeneous nucleation and adsorption, Philos. Trans. R. Soc. London A. 361 (2003) 409–417.
[11] C.M. Fang, H. Men, Z. Fan, Effect of substrate chemistry on prenucleation, Metall. Mater. Trans. A. 49 (2018) 6231–6242.
[12] C.M. Fang, Z. Fan, Prenucleation at the interface between MgO and liquid magnesium: an ab initio molecular dynamics study, Metall. Mater. Trans. A. 51 (2020) 788–797.
[13] Y. Wang, C.M. Fang, L. Zhou, T. Hashimoto, X. Zhou, Q.M. Ramasse, Z. Fan, Mechanism for Zr poisoning of Al-Ti-B based grain refiners, Acta Mater 164 (2019) 428–439.

[14] Y. Li, B. Hu, B. Liu, A. Nie, Q. Gu, J. Wang, Q. Li, Insight into Si poisoning on grain refinement of Al-Si/Al-5Ti-B system, Acta Mater 187 (2020) 51–65.
[15] D.L. Zhang, B. Cantor, Effect of Ge on the heterogeneous nucleation of Pb solidification by Al, J. Cryst. Growth. 104 (1990) 583–592.
[16] C.R. Ho, B. Cantor, Effect of Ge on the heterogeneous nucleation of Cd solidification by Al, Philos. Mag. A. 66 (1992) 141–149.
[17] B. Jiang, H. Men, Z. Fan, Atomic ordering in the liquid adjacent to an atomically rough solid surface, Comput. Mater. Sci. 153 (2018) 73–81.
[18] J.W. Gibbs, The scientific papers of J. Willard Gibbs, Longmans, Green and Company, 1906.
[19] P. Wynblatt, Interfacial Segregation Effects in Wetting Phenomena, Annu. Rev. Mater. Res. 38 (2008) 173–196.
[20] W.D. Kaplan, D. Chatain, P. Wynblatt, W.C. Carter, A review of wetting versus adsorption, complexions, and related phenomena: The rosetta stone of wetting, J. Mater. Sci. 48 (2013) 5681–5717.
[21] G.S. Peng, Y. Wang, K.H. Chen, S.Y. Chen, Improved Zr grain refining efficiency for commercial purity Mg via intensive melt shearing, Int. J. Cast Met. Res. 30 (2017) 374–378.
[22] P. Schumacher, A.L. Greer, High-resolution transmission electron microscopy of grain-refining particles in amorphous aluminum alloys, in: Hale Wayne (Ed.), Light Met. 1996, Minerals, Metals & Materials Soc (TMS), 1996, pp. 745–753. Warrendale, PA (United States).
[23] A.M. Bunn, P. Schumacher, M.A. Kearns, C.B. Boothroyd, A.L. Greer, Grain refinement by Al-Ti-B alloys in aluminium melts: a study of the mechanisms of poisoning by zirconium, Mater. Sci. Technol. 15 (1999) 1115–1123.
[24] P. Schumacher, B.J. McKay, TEM investigation of heterogeneous nucleation mechanisms in Al–Si alloys, J. Non. Cryst. Solids. 317 (2003) 123–128.
[25] Z. Fan, Y. Wang, Y. Zhang, T. Qin, X.R. Zhou, G.E. Thompson, T. Pennycook, T. Hashimoto, Grain refining mechanism in the Al/Al-Ti-B system, Acta Mater 84 (2015) 292–304.
[26] Y. Wang, Z. Que, T. Hashimoto, X. Zhou, Z. Fan, Mechanism for Si Poisoning of Al-Ti-B Grain Refiners in Al-Alloys, Metall. Mater. Trans. A. 51 (2020) 5743–5757.
[27] S.H. Wang, F. Wang, Y. Wang, Q.M. Ramasse, Z. Fan, Segregation of Ca at the Mg/MgO interface and its effect on grain refinement of Mg alloys, IOP Conf. Ser. Mater. Sci. Eng. 529 (2019), 012048.
[28] Z. Fan, Y. Wang, M. Xia, S. Arumuganathar, Enhanced heterogeneous nucleation in AZ91D alloy by intensive melt shearing, Acta Mater 57 (2009) 4891–4901.
[29] Y. Wang, Z. Fan, X. Zhou, G.E.E. Thompson, Characterisation of magnesium oxide and its interface with α-Mg in Mg-Al-based alloys, Philos. Mag. Lett. 91 (2011) 516–529.
[30] S. Wang, Y. Wang, Q. Ramasse, Z. Fan, The nature of native MgO in Mg and its alloys, Metall. Mater. Trans. A. 51 (2020) 2957–2974.
[31] H. Hall, A note on attempts to produce superheating effect by addition of alumina to electron A-8, Magnes. Rev. Abs. 3 (1945) 68.
[32] Y. Wang, G. Peng, Z. Fan, Grain refinement of mg and its alloy by inoculation of in situ MgO particles, in: K.N. Solanki, D. Orlov, S. Alok, N.R. Neelameggham (Eds.), Magnes. Technol., Springer, 2017, pp. 99–106, 2017.
[33] L. Rogal, L. Litynska-Dobrzynska, Effect of in-situ formed MgO on the microstructure of thixomolded AZ91 magnesium alloy, Mater. Sci. Technol. (United Kingdom) 35 (2019) 349–360.
[34] Z. Fan, F. Gao, B. Jiang, Z. Que, Impeding nucleation for more significant grain refinement, Sci. Rep. 10 (2020) 1–11.
[35] H. Men, B. Jiang, Z. Fan, Mechanisms of grain refinement by intensive shearing of AZ91 alloy melt, Acta Mater 58 (2010) 6526–6534.
[36] G.S. Peng, G.S. Song, Y. Wang, K.H. Chen, S.Y. Chen, Intensive melt shearing and calcium concentration effects on grain refinement of commercial purity Mg, Int. J. Cast Met. Res. 31 (2018) 99–107.
[37] Y.C. Lee, Grain Refinement of Magnesium, The University of Queensland, 2002. PhD thesis.
[38] Y. Kawamura, K. Hayashi, A. Inoue, T. Masumoto, Rapidly solidified powder metallurgy Mg97Zn1Y2 alloys with excellent tensile yield strength above 600 MPa, Mater. Trans. 42 (2001) 1172–1176.
[39] S. Sandlöbes, M. Friák, S. Zaefferer, A. Dick, S. Yi, D. Letzig, Z. Pei, L.F. Zhu, J. Neugebauer, D. Raabe, The relation between ductility and stacking fault energies in Mg and Mg-Y alloys, Acta Mater 60 (2012) 3011–3021.
[40] M. Suzuki, H. Sato, K. Maruyama, H. Oikawa, Creep behavior and deformation microstructures of Mg-Y alloys at 550 K, Mater. Sci. Eng. A. 252 (1998) 248–255.
[41] H.B. Yao, Y. Li, A.T.S. Wee, Passivity behavior of melt-spun Mg-Y Alloys, Electrochim. Acta. 48 (2003) 4197–4204.
[42] M. Sun, D.H. StJohn, M.A. Easton, K. Wang, J. Ni, Effect of cooling rate on the grain refinement of Mg-Y-Zr Alloys, Metall. Mater. Trans. A. 51 (2020) 482–496.
[43] J. Li, R. Chen, Y. Ma, W. Ke, Effect of Zr modification on solidification behavior and mechanical properties of Mg-Y-RE (WE54) alloy, J. Magnes. Alloy. 1 (2013) 346–351.
[44] A.A. Association, Standard test procedure for aluminum alloy grain refiners, Alum. Assoc. (2012).
[45] M. Watanabe, M. Kanno, D. Ackland, C. Kiely, D. Williams, Applications of electron energy-loss spectrometry and energy filtering in an aberration-corrected JEM-2200FS STEM/TEM, Microsc. Microanal. 13 (2007) 2006–2007.
[46] C.T. Koch, Determination of Core Structure Periodicity and Point Defect Density Along Dislocations, Arizona State University, 2002. PhD thesis.
[47] Y. Zeng, B. Jiang, M.X. Zhang, H. Yin, R. Li, F. Pan, Effect of Mg24Y5 intermetallic particles on grain refinement of Mg-9Li alloy, Intermetallics 45 (2014) 18–23.
[48] J. Narayan, B.C. Larson, Domain epitaxy: A unified paradigm for thin film growth, J. Appl. Phys. 93 (2003) 278–285.
[49] M. Boiocchi, F. Caucia, M. Merli, D. Prella, L. Ungaretti, Crystal-chemical reasons for the immiscibility of periclase and wüstite under lithospheric P,T conditions, Eur. J. Mineral. 13 (2001) 871–881.
[50] S. Katagiri, N. Ishizawa, F. Marumo, A new high temperature modification of face-centered cubic Y2O3, Powder Diffr 8 (1993) 60.
[51] Y. Ali, G. You, F. Pan, M.X. Zhang, Grain coarsening of cast magnesium alloys at high cooling rate: a new observation, Metall. Mater. Trans. A. 48 (2017) 474–481.
[52] C.C. Ahn, O.L. Krivanek, M.M. Disko, EELS Atlas: A Reference Collection of Electron Energy Loss Spectra Covering All Stable Elements, HREM Facility, Center for Solid State Science, Arizona State University, 1983.
[53] P.R. Cantwell, M. Tang, S.J. Dillon, J. Luo, G.S. Rohrer, M.P. Harmer, Grain boundary complexions, Acta Mater 62 (2014) 1–48.
[54] S.J. Dillon, M. Tang, W.C. Carter, M.P. Harmer, Complexion: a new concept for kinetic engineering in materials science, Acta Mater 55 (2007) 6208–6218.
[55] F.Y. Cui, A. Kundu, A. Krause, M.P. Harmer, R.P. Vinci, Surface energies, segregation, and fracture behavior of magnesium aluminate spinel low-index grain boundary planes, Acta Mater 148 (2018) 320–329.
[56] C.J. Marvel, A.R. Krause, M.P. Harmer, Effect of Eu-doping and grain boundary plane on complexion transitions in MgAl2O4, J. Am. Ceram. Soc. 104 (2021) 4203–4213.
[57] H. Men, Z. Fan, An analytical model for solute segregation at liquid metal/solid substrate interface, Metall. Mater. Trans. A. 45 (2014) 5508–5516.
[58] O.B. Fabrichnaya, H.L. Lukas, G. Effenberg, F. Aldinger, Thermodynamic optimization in the Mg-Y system, Intermetallics 11 (2003) 1183–1188.
[59] W. Cao, S. Chen, F. Zhang, K. Wu, Y. Yang, Y.A. Chang, R. Schmid-fetzer, W. A. Oates, PANDAT software with PanEngine, PanOptimizer and PanPrecipitation for multi-component phase diagram calculation and materials property simulation, CALPHAD Comput. Coupl. Phase Diagrams Thermochem. 33 (2009) 328–342.
[60] R. Schmid-Fetzer, F. Zhang, The light alloy Calphad databases PanAl and PanMg, Calphad Comput. Coupl. Phase Diagrams Thermochem. 61 (2018) 246–263.
[61] J. Goniakowski, C. Noguera, Microscopic mechanisms of stabilization of polar oxide surfaces: transition metals on the MgO (111) surface, Phys. Rev. B. 66 (2002), 085417.
[62] J.P. Buban, K. Matsunaga, J. Chen, N. Shibata, W.Y. Ching, T. Yamamoto, Y. Ikuhara, Grain boundary strengthening in alumina by rare earth impurities, Science 311 (2006) 212–215.
[63] J.D. Robson, S.J. Haigh, B. Davis, D. Griffiths, Grain boundary segregation of rare-earth elements in magnesium alloys, Metall. Mater. Trans. A. 47 (2016) 522–530.
[64] Y.-R. Luo, J.A. Kerr, Bond dissociation energies, CRC Handb, Chem. Phys. 89 (2012) 89.
[65] E. Clementi, D.L. Raimondi, W.P. Reinhardt, Atomic screening constants from SCF functions. II. Atoms with 37 to 86 electrons, J. Chem. Phys. 47 (1967) 1300–1307.
[66] B.L. Bramfitt, The effect of carbide and nitride additions on the heterogeneous nucleation behavior of liquid iron, Metall. Trans. 1 (1970) 1987–1995.
[67] W. Xu, R. Zheng, K.J. Laws, S.P. Ringer, M. Ferry, In situ formation of crystalline flakes in Mg-based metallic glass composites by controlled inoculation, Acta Mater 59 (2011) 7776–7786.
[68] T.F. Tadros, Dispersion of Powders: in Liquids and Stabilization of Suspensions, John Wiley & Sons, 2012.